# The Daya Bay Reactor Neutrino Experiment

YuenKeung Hor

Dissertation submitted to the Faculty of the
Virginia Polytechnic Institute and State University
in partial fulfillment of the requirements for the degree of

Doctor of Philosophy in Physics

Jonathan M. Link (Chair)
Camillo Mariani
Patrick Huber
Eric R. Sharpe

August 8, 2014
Blacksburg, Virginia



Keywords: muon veto, anti-neutrino detector, attenuation length, spent fuel neutrino, reactor spectrum

# The Daya Bay Reactor Neutrino Experiment

YuenKeung Hor

(ABSTRACT)

The Daya Bay experiment has determined the last unknown mixing angle $\theta_{13}$. This thesis describes the layout of the experiment and the detector design. The analysis presented in the thesis covered the water attenuation, spent fuel neutrino and electron anti-neutrino spectrum. Other physics analysis and impact to future experiments are also discussed.

For the day I have been dreaming in 30 years,

Today is the day.

# Acknowledgments

My first visit to Daya Bay power plant was in 2002 when i was in high school. For the 8 years i have been working on the Daya Bay project since 2006, i met many talented technicians, engineers and physicists in the experiment. Of all the priceless memories, I would like to thank the following persons:

Jo Ellen and Kim for our daily gossip.
Mengyun, Jilei, zhenglei and huifeng for efforts on RPC and every drop of liquor we shared.
Dan, Yasu, jiajie and weili for their analysis advice.
Special thank to Evan for our countless beers.

The members of dissertation committee: Prof. Mariani, Prof. Huber and Prof. Sharpe.
Prof. Chu for my Master degree training.
Prof. Luk for all his help along my academic path.
Prof. Link for his role as an advisor and as a physicist.

Dr. Yue, Meng for our romance.
Friends who believe in me all the years: Winnie Leung, Kit Wong, Jacky Lo, Edward Lam.
My mom, brother, sister, niece and nephew for their support and smiles.
And many for whom i shall thank in person.

# Contents

# List of Figures

# List of Tables

# Chapter 1

# Introduction

## 1.1 Standard Model

The Standard Model(SM)[1] of particle physics is a description of fundamental particles and interactions based on theory and constraints from experimental observations. In the SM, all matter is made out of three kinds of elementary particles: leptons, quarks and mediators.[2]. The leptons, being fundamental with no detectable internal structures, are classified according to their charge($Q$) and lepton family numbers($L_e$, $L_\mu$, $L_\tau$). The three generations come with two leptons apiece. Table 1.1 showed the lepton classification. The anti-particles of leptons are those with opposite sign to their lepton numbers since they could be charge neutral.

There are also six quarks, up and down, strange and charm, top and bottom, classified by charge. Similar to the leptons classification, quarks fall into three generations, and there are six antiquarks, each with the sign of their charge reversed. The four basic interactions: gravitational, electromagnetic, strong and weak, mediated through all reaction dynamics by exchanging fundamental gauge bosons. For each type of interaction, there is at least one such force carrier particle that mediates the interaction. Table 1.2 shows the properties of the interactions.

| | | $Q$ | $L_e$ | $L_\nu$ | $L_\tau$ |
|---|---|---|---|---|---|
| First | $e$ | -1 | 1 | 0 | 0 |
| Generation | $\nu_e$ | 0 | 1 | 0 | 0 |
| Second | $\mu$ | -1 | 0 | 1 | 0 |
| Generation | $\nu_\mu$ | 0 | 0 | 1 | 0 |
| Third | $\tau$ | -1 | 0 | 0 | 1 |
| Generation | $\nu_\tau$ | 0 | 0 | 0 | 1 |

Table 1.1: Lepton classification

| Interactions | Mediator | Acts on |
|---|---|---|
| Gravitational | Graviton | Mass |
| Weak | $W^+, W^-, Z^0$ | Flavor |
| Electromagnetic | $\gamma$ | Electric charge |
| Strong | 8 gluons | Color charge |

Table 1.2: Properties of the four interactions

The concept of neutrino was postulated by Pauli in 1930, based on Charles Ellis and James chadwick's experiment confirming the continuous energy spectrum[3] in nuclear beta decay($n \to p^+ + e^- + \overline{\nu}$), as shown in fig. 1.1

In 1946, Bruno Pontecorvo identified nuclear reactors as an intense and pure source of neutrino[4, 5]. In 1953, an attempt to detect neutrinos in Hanford, with 300kg of cadmium doped liquid scintillator, was inconclusive due to low signal to background ratio. Later in 1956, the decisive experiment was conducted at the Savannah River nuclear reactor in South Carolina. Cowan and Reines[6] set up a large tank of cadmium salt-loaded water and watched for the inverse beta decay reaction($\overline{\nu} + p^+ \to n + e^+$)[2]. The result convincingly

confirmed the existence of neutrinos, as shown in fig. 1.2.

At the time the SM was constructed, neutrinos were assumed to be massless. This is now known to disagree with observations of flavor oscillation in multiple experiments which demands that neutrinos have small but distinct masses among all flavors.

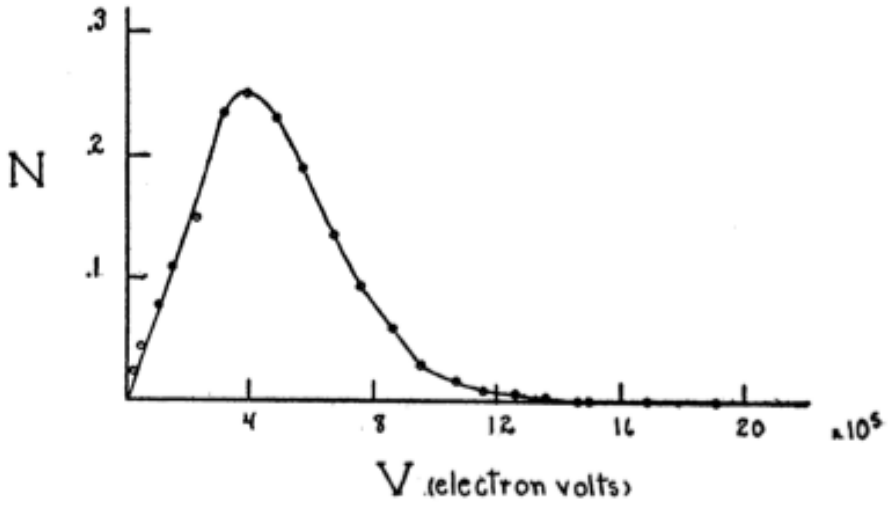


FIG. 5. Energy distribution curve of the beta-rays.

Figure 1.1: The continuous spectrum of electron in beta-decay of Radium[3].

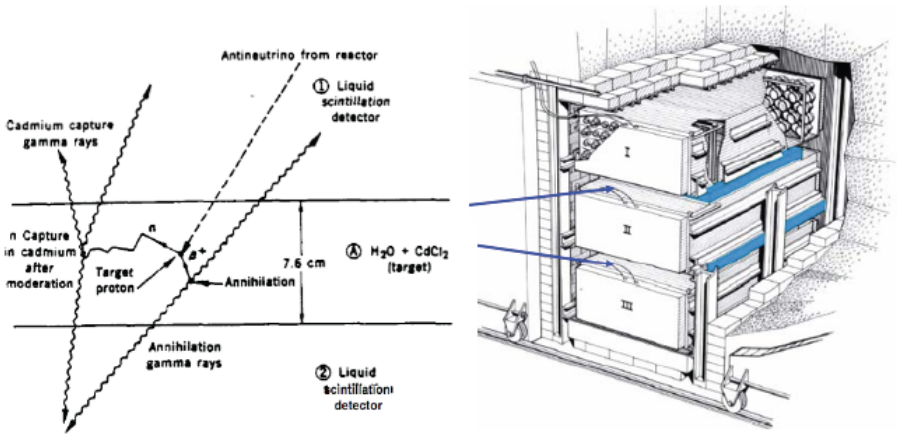


Figure 1.2: Cowan and Reines's experiment in Savannah River[6].

## 1.2 Reactor Neutrino Experiment

The chlorine based Homestake experiment led to a puzzle to the particle community[7], known as the solar neutrino problem. The issue was that the experiment only observed about one third of the expected neutrinos from the Sun, as modeled and predicted by J. Bahcall[8]. The physics of the Standard Solar Model(SSM) has not been well agreed by that time and therefore the results of the Homestake experiment triggered discussion.

There were many attempts to resolve the solar neutrino problem which included modifications to the SSM and criticisms against the Homestake experiment. Bruno Pontecorvo proposed, in 1968[9], in contrast to what was generally believed and imposed in SM, that neutrinos could have mass and this neutrino mass could potentially explain the neutrino deficit between SSM and data. However, this hypothesis was not validated by experiment until late 90's.

The first strong evidence came from the Super-Kamiokande in Japan in 1998[10]. It is an experiment designed to observe the oscillation from $\nu_\mu$ to $\nu_e$ as a function of path length and energy. SuperK compared the observation of atmospheric muon-type neutrinos, generated by cosmic ray, through two paths. One is the muon neutrinos hitting into the underground detector directly from the atmosphere, while another path is the muon neutrino going through

the crust of Earth to the detector. The difference, shown in fig.1.3 , suggested that some muon neutrinos from long path length were missing and this was due to oscillation of $\nu_\mu$ into $\nu_\tau$, which were not observed in their detector.

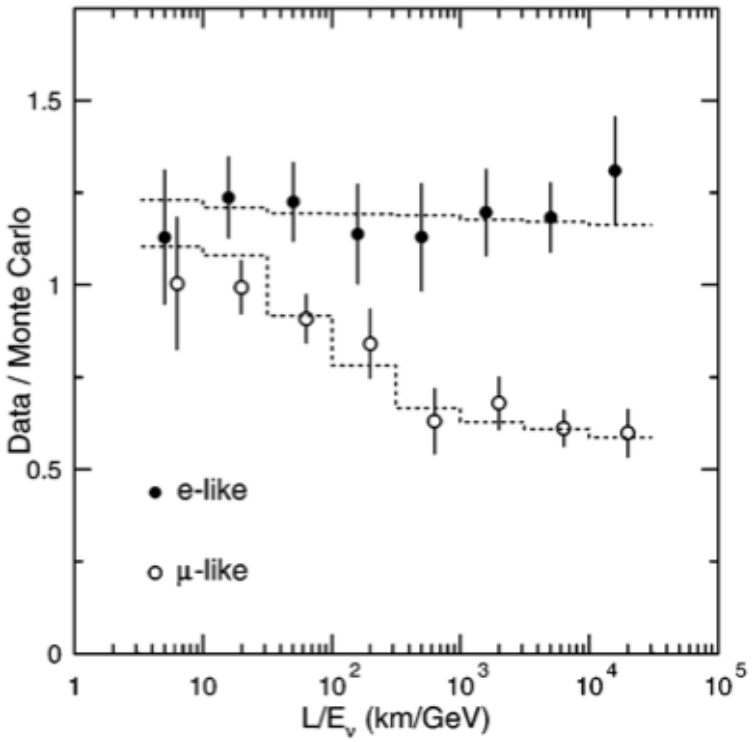


Figure 1.3: Indication of oscillation by comparing data to MC of no oscillation[10]

The defining observation of solar neutrino oscillation came from the Sudbury neutrino observatory(SNO) in Canada in 2001[11]. It was designed to measure the flux of the three neutrino flavors using a mix of charged and neutral current interactions in heavy water. In particular, it could distinguish the electron-type from the remaining two. The measurement determined that 35% of the solar neutrino flux are electron-type neutrinos while the total number of detected neutrinos agrees with the SSM prediction. It was this measurement, shown in fig.1.4 that confirmed the neutrino oscillation hypothesis and resolved the solar neutrino problem.

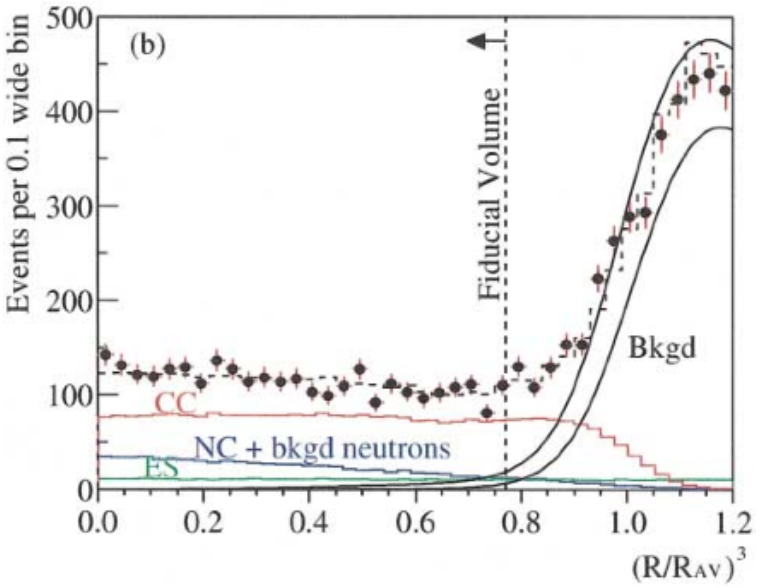


Figure 1.4: Confirmation of flavor oscillation from Sudbury Neutrino Observatory[11].

## 1.3 Neutrino Oscillation

The solar neutrino problem was developed from the measured disparity between the standard solar model prediction and the experimental measurement by Ray Davis in Homestake mine in South Dakota(1968). Later Bruno Pontecorvo proposed the concept of neutrino oscillation to explain the solar neutrino problem. Neutrino oscillation is a quantum mechanical phenomenon, which the quantum wave packet of one flavor oscillates and interferes with other flavors when traveling through the space. The interference is straightened once a measurement is attempted to determine the oscillating flavor at the measurement position. Let us consider how flavor mixing affects the propagation of neutrino in vacuum. We take the initial state to be the flavor eigenstate[12],

$$|\nu_\alpha(0)\rangle = U^*_{\alpha j} |\nu_j\rangle \tag{1.1}$$

Here and in the following we denote flavor eigenstates $(e, \mu, \tau)$ by Greek indices and mass eigenstates (1, 2, 3) by Latin indices. After time $t$ and distance $x$, the state has evolved into

$$|\nu_\alpha(t)\rangle = U^*_{\alpha j} e^{-i(E_j t - p_j x)} |\nu_j\rangle \tag{1.2}$$

where $E_j$ and $p_j$ are the energy and momentum associated with the mass eigenstate $j$. They can be derived from the dynamics of the elementary process in which the neutrino is produced. For example, in the case of pion decay at rest, $\pi^\pm \to \mu^\pm + \nu_\mu/\bar{\nu_\mu}$, we have in the centre of mass system

$$m_\pi = E_j + E_j = \sqrt{m_j^2 + p_j^2} + \sqrt{m_\mu^2 + p_\mu^2} \tag{1.3}$$

$$p_\mu = -p_\mu \tag{1.4}$$

Substitute Eq.(1.4) into Eq.(1.3) and taking the square. We simplify the expressions for $p_j^2, E_j^2$.

$$p_j^2 = \frac{m_\pi^2}{4}\left(1-\frac{m_\mu^2}{m_\pi^2}\right)^2 - \frac{m_j^2}{2}\left(1+\frac{m_\mu^2}{m_\pi^2}\right) + \frac{m_j^4}{4m_\pi^2} \tag{1.5}$$

$$E_j^2 = \frac{m_\pi^2}{4}\left(1-\frac{m_\mu^2}{m_\pi^2}\right)^2 + \frac{m_j^2}{2}\left(1-\frac{m_\mu^2}{m_\pi^2}\right) + \frac{m_j^4}{4m_\pi^2} \tag{1.6}$$

By denoting the energy that would be obtained for massless neutrinos by $E = \frac{m_\pi}{2}(1-m_\mu^2/m_\pi^2)$ and keeping only terms up to second order in $m_j$,

$$p_j = E - \frac{m_j^2}{2E}\left(\frac{1}{2}+\frac{m_\mu^2}{2m_\pi^2}\right) = E - \frac{m_j^2}{2E}\zeta \tag{1.7}$$

$$E_j = E + \frac{m_j^2}{2E}\left(1-\left[\frac{1}{2}+\frac{m_\mu^2}{2m_\pi^2}\right]\right) = E + \frac{m_j^2}{2E}(1-\zeta) \tag{1.8}$$

If the neutrino is produced in some other process than pion decay, $\zeta$ will be different, but the general structure of the equations remains the same. The exponent in the neutrino evolution Eq.(1.2) can now be rewritten as,

$$E_j t - p_j x = Et + \frac{m_j^2}{2E}(1-\zeta)t - Ex + \frac{m_j^2}{2E}\zeta x \tag{1.9}$$

Although the group speeds of the neutrino wave packets differ from the speed of light by terms of order $m_j^2$, the time resolution in a realistic experiment is too poor to resolve this difference. Therefore quantum mechanical uncertainty justifies taking $x = t$(except for very long baseline such as supernova). Thus the terms proportional to $\zeta$ drop out, and we simply have,

$$|\nu(t)\rangle = U_{\alpha j}^* e^{-im_j^2 t/2E}\,|\nu_j\rangle \tag{1.10}$$

From this, the neutrino oscillation probability is obtained as

$$P(\nu_\alpha \to \nu_\beta) = |\,\langle\nu_\beta|\nu(t)\rangle\,|^2 = |U_{\beta j}U_{\alpha j}^* e^{-im_j^2 t/2E}|^2 \tag{1.11}$$

The typical Schrödinger ansatz is not strictly correct because the $\zeta$-term in the energy eigenvalue in Eq.(1.8) is neglected in the approach. Furthermore, the x-dependence of the

wave functions is omitted so that effectively all momenta $p_j$ are assumed to be equal and thus the $\zeta$ term in Eq.(1.7) is neglected as well. However, the more accurate derivation leading to the final result shows the combination of these two simplification leads to the correct result since the $\zeta$ drops out anyway.

Furthermore, putting back $\alpha, \beta$ to three types of neutrino flavors and approximating distance travelled by $L = ct$ give

$$P(\nu_{l_a} \to \nu_{l_a}) = 1 - \sin^2 2\theta \sin^2(1.267 \times \frac{\Delta m^2[eV^2] \times L[km]}{E[GeV]}) \tag{1.12}$$

Formula 1.12 gives the sensitivity of an experiment in terms of practical units. An experiment aims to be sensitive to one parameter, then the combination of other parameters is needed to be adjusted.

Expanding to three flavor neutrino oscillations, one gets a 3x3 mixing matrix called Pontecorvo-Maki-Nakagawa-Sakata matrix(PMNS)[13], analogous to the Cabibbo-Kobayashi-Maskawa matrix(CKM) in quarks mixing case[2], such that:

$$\begin{pmatrix} \nu_e \\ \nu_\mu \\ \nu_\tau \end{pmatrix} = U_{PMNS} \begin{pmatrix} \nu_1 \\ \nu_2 \\ \nu_3 \end{pmatrix}$$

$$U_{PMNS} = \begin{pmatrix} c_{12}c_{13} & s_{12}c_{13} & s_{13}e^{-i\delta} \\ -s_{12}c_{23} - c_{12}s_{23}s_{13}e^{i\delta} & c_{12}c_{23} - s_{12}s_{23}s_{13}e^{i\delta} & s_{23}c_{13} \\ s_{12}s_{23} - c_{12}c_{23}s_{13}e^{i\delta} & -c_{12}s_{23} - s_{12}c_{23}s_{13}e^{i\delta} & c_{23}c_{13} \end{pmatrix}$$

where $c_{ij} \equiv \cos\theta_{ij}, s_{ij} \equiv \sin\theta_{ij}$. $\theta_{ij}$ represents the mixing angle and $\delta$ is the CP phase factor. Past experiments detecting atmospheric and solar neutrinos as well as using accelerator had been able to measure all the mixing angles except $\theta_{13}$ to high precision. Long baseline accelerator experiment is also capable of making the CP measurement in the future depending on the absolute size of $\theta_{13}$. Currently ongoing reactor experiments such as Daya Bay, RENO[14] and Double Chooz[15] are dedicated to measure this angle and possibly determining the mass hierarchy.

## 1.4 Summary

After the first discovery of neutrinos from Cowan and Reine's Savannah river experiment, the existence of the originally "undetectable" particle resolved the beta decay energy spectrum issue. At the same time it created more questions to challenge the community over the last 50 years including but not limited to the solar problem. More experiments were proposed and constructed to determine various properties of neutrinos from sources such as reactors, the atmosphere, accelerators and the Sun. Detection technique have been improving from reducing backgrounds by shielding to enhancing reaction cross-section by chemical doping. Though the SM has been successful in describing many basic interactions and in predicting new particles, it failed to note that neutrino have mass and therefore their oscillation behavior. Mixing angles in the PMNS matrix have been consequently determined by various experiments using neutrinos from different sources but not all parameters have yet been identified. To better understand oscillation phenomena, especially to unveil the last unknown mixing angle in the PMNS matrix, a reactor neutrino experiment was the ideal choice because of its intense, pure electron anti-neutrino flux in well controlled operation and the feasibility to build detectors at short baselines.

# Chapter 2

# The Daya Bay Reactor Neutrino Experiment

## 2.1 Motivation

Experiments on neutrinos originating from the atmosphere[10], the Sun[8]and multiple nuclear reactors[6] have been successful in validating the oscillation phenomenon and calculating most of the mixing angles in the PMNS matrix. The disadvantage of all those experiments, however, is that distance from the source to detector is very long as compared with the oscillation length(with reference to equation 1.10), hindering them from measuring the detailed shape of oscillation. Accelerator experiments, on the other hand, are feasible in shorter baselines, but the neutrino beam is usually mixed in all flavors and make a disappearance measurement analysis very complicated.

In order to clearly observe the oscillation pattern, reactor neutrino experiments around the world are proposed at various baselines from active commercial reactors. The advantages of reactor experiment are:

• Pure source of electron anti-neutrinos, with energy known from beta-decays

• Intense isotropic source, about $6 \times 10^{20}$ neutrino per second for a 3 GW reactor

• Direct measurement of backgrounds during reactor downtime[15]

• Known operations and reactor information

With all these advantages, several reactor neutrino experiments have been recently running with short baselines to measure the last mixing angle $\theta_{13}$ using multiple detectors.

## 2.2 Recent Reactor Neutrino Experiments

Several reactor experiments around the world attempted to observe oscillation after Hanford and the Savannah river have made significant contributions to the field. The following subsections briefly described some of the settings and results.

### 2.2.1 Institut Laue-Langevin (ILL)

Given the solar neutrino deficit, the ILL reactor neutrino experiment set out to test whether there was a related deficit of reactor neutrinos. A 57 MW thermal power reactor at ILL in Grenoble of France was used as the $\bar{\nu}_e$ source. The detector consisted of a sandwich of 5 planes of liquid scintillator contained in acrylic and four $^3He$ wire counter planes for neutron detection. A total scintillator target volume of 377 L corresponding to 2.39 x $10^{28}$ target protons was used. The detector was placed 8.76 m from the reactor core, with an expected $\bar{\nu}_e$ flux of 9.8 x $10^{11}$ $cm^{-2}s^{-1}$ at the detector. A total of 4890 $\pm$ 180 antineutrino events were detected at a rate of 1.58 $h^{-1}$. The ratio of detected to expected events was measured and found to be consistent with the predicted flux,[16, 17]

$$R = 0.955 \pm 0.035(stat.) \pm 0.110(sys.) \tag{2.1}$$

### 2.2.2 Bugey

The Bugey experiment measured the antineutrino flux from a 2800 MW thermal power reactor[18]. Early results showed evidence of neutrino oscillation which was inconsistent with other experiments[19]. After further control of systematic uncertainties, an improved experiment used three identical detectors, one at 15 m directly beneath the core of the reactor and the other two at 40 m. during a shutdown period of one reactor, the near detector was used to measure the $\bar{\nu}_e$ flux from a second reactor operating 95 m away. Each detector consisted of 600 L of liquid scintillator loaded with 0.15% of $^6Li$ by mass, and divided into 98 segments. the delayed neutron was detected using the reaction,

$$n +^6 Li \rightarrow^4 He +^3 H + 4.8MeV \tag{2.2}$$

About 120,000 total inverse beta decay events were detected. At each location, the number of detected events was consistent with the expected number of events with no oscillation[18],

$$R_{15} = 0.988 \pm 0.004(stat.) \pm 0.05(sys.) \tag{2.3}$$

$$R_{40} = 0.994 \pm 0.010(stat.) \pm 0.05(sys.) \tag{2.4}$$

$$R_{95} = 0.915 \pm 0.132(stat.) \pm 0.05(sys.) \tag{2.5}$$

### 2.2.3 Chooz

In an attempt to reach even greater sensitivity to long oscillation lengths, the CHOOZ experiment measured the electron antineutrino flux at 1 km from two reactor cores. the two reactors, located near the village of Chooz in the Ardennes region of France, had a total thermal power of 8.5 GW. The detector size was drastically increased to compensate the inverse square distance loss[20]. The Chooz detector consisted of a 5 ton target of liquid scintillator, loaded with 0.09% of gadolinium(Gd). Neutron capture on Gd produces a set of gamma rays with a total energy of about 8 MeV. With a lower $\bar{\nu}_e$ flux and larger target

volume than previous experiments, backgrounds were suppressed by placing the detector underground with rock shielding of 300 meters water equivalent(m.w.e.)
A total of 2991 coincidence events were collected from April 1997 until July 1998 and backgrounds was measured during the reactor shutdown period. The ratio of detected events to expected events with no oscillation was found to be[21]:

$$R = 1.01 \pm 0.028(stat.) \pm 0.027(sys.) \tag{2.6}$$

### 2.2.4 Palo Verde

Palo Verde was an experiment to measure the $\bar{\nu}_e$ flux at the Palo Verde Nuclear Generating Station in Arizona. The facility consisted of three cores with a total thermal power of 11.63 GW. The single detector was placed 750 m from one core and 890 m from the other two, shielded by rock of 32 m.w.e. The detector was a 11.34 tons of liquid scintillator divided into 66 optically isolated segments. It was loaded with 0.1% Gd for neutron capturing. The measured to expected event ratio was[22],

$$R = 1.01 \pm 0.024(stat.) \pm 0.053(sys.) \tag{2.7}$$

### 2.2.5 KamLAND

KamLAND stands for Kamioka Liquid Scintillator Anti-Neutrino Detector. The experimental site is surrounded by 55 Japanese nuclear power reactor units. Out of the many reactors, 79% of the computed flux arose from just 26 reactors within the distance range 138-214 km. The detector is a 1 kton liquid scintillator contained in a 13 m diameter spherical balloon located underground with 2300 m.w.e of rock. The results of the experiment confirmed the solar neutrino oscillation and the measured oscillation parameter $\theta_{12}$[23]. The ratio of observed events to expected events is:

$$R = 0.611 \pm 0.085(stat.) \pm 0.041(sys.) \tag{2.8}$$

Combining the data from reactor and solar neutrinos, KamLAND also published a results on the mass square difference and the mixing angle to be[24],

$$\Delta m^2_{21} = 7.58^{+0.14}_{-0.13}(stat.)^{+0.15}_{-0.15}(sys.) \times 10^{-5} eV^2 \quad (2.9)$$

$$\tan^2\theta_{12} = 0.56^{+0.10}_{-0.07}(stat.)^{+0.10}_{-0.06}(sys.) \quad (2.10)$$

Figure 2.1 shows the oscillation pattern measured by KamLAND.

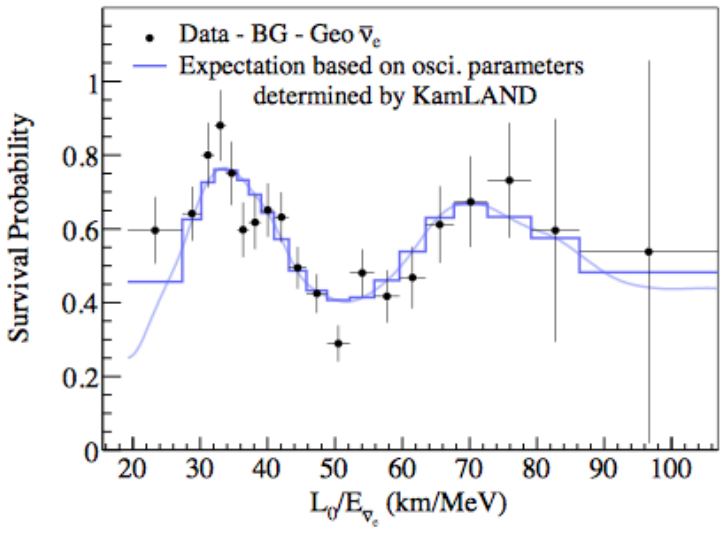


Figure 2.1: The measured oscillation pattern of KamLAND in terms of energy and baselines[24].

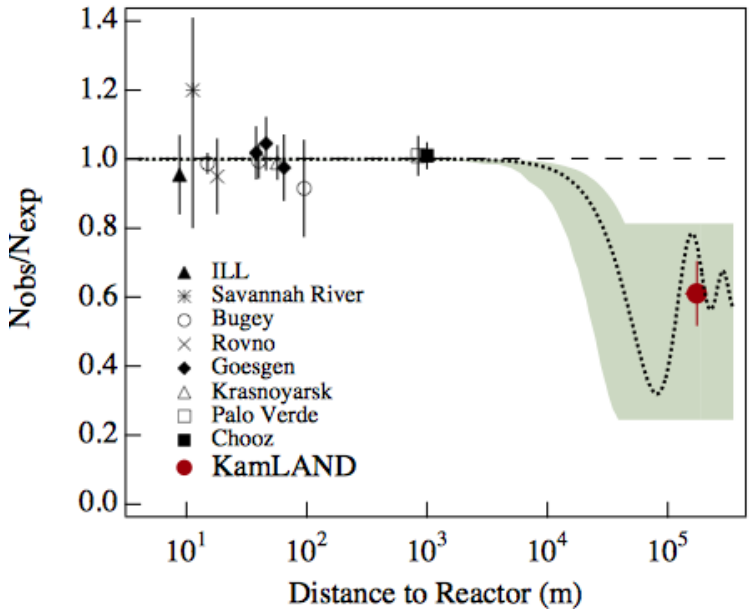


Figure 2.2: Ratio of detected events to expected events versus distance of previous experiments. Oscillation was best demonstrated by KamLAND[23].

With the effort from all the above experiments and others, a direct oscillation pattern and values of the neutrino mass mixing parameters have been reported by KamLAND neutrino flux measurement have been done by ILL and Bugey and constraints have been set on the value of $\theta_{13}$ which will be discussed in the next section.

## 2.3 The Daya Bay Experiment

The Daya Bay reactor power plant complex is located in southern China, about 60 km northeast of Hong Kong. The reactor complex consisted of three pairs of pressurized water reactor cores with a total thermal power of 17.4 GW. The reactor layout is shown in 2.3.

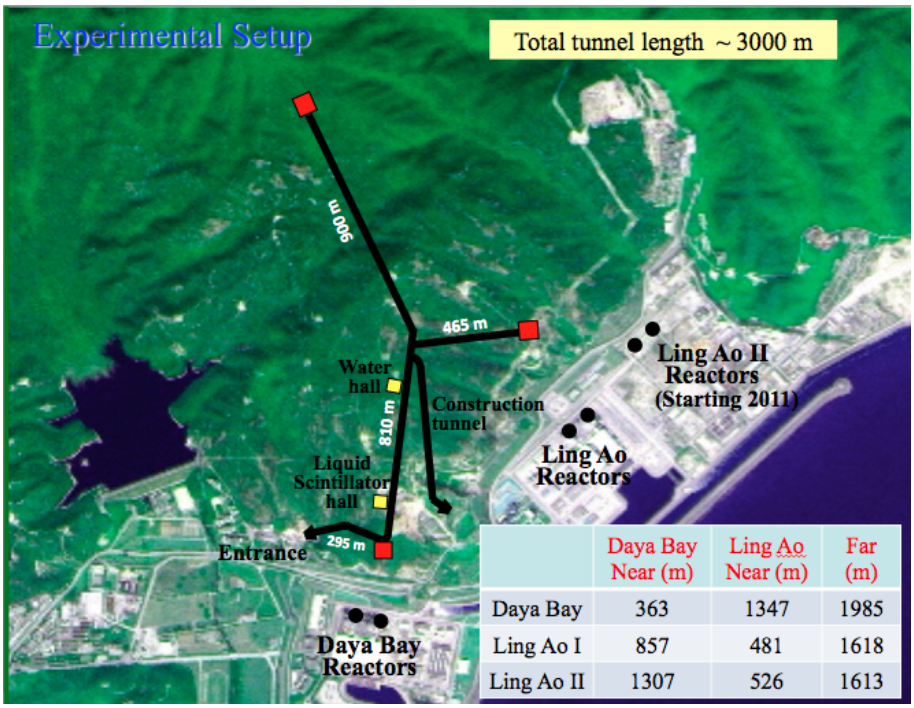


| | Daya Bay Near (m) | Ling Ao Near (m) | Far (m) |
|---|---|---|---|
| Daya Bay | 363 | 1347 | 1985 |
| Ling Ao I | 857 | 481 | 1618 |
| Ling Ao II | 1307 | 526 | 1613 |

Figure 2.3: The reactor layout of Daya Bay experiment. Black lines are tunnel to each site and the table showed the baselines from 3 pairs of cores to each site.

In addition to its high thermal power, the mountain profile of the ridge roughly 300 m away from the complex provides enough rock overburden to reduce cosmic muons and their induced backgrounds. To observe the oscillation, three experimental sites have been built to compare the neutrino flux at different baselines based on measured events. These are the Daya Bay Near site(DYB Near), Ling Ao Near site(LA Near) and the Far site.

The location of each site is an optimization of sensitivity to $\sin^2 2\theta_{13}$ based on distances. The sensitivity of the experiment depends on the size of $\theta_{13}$ and the mass squared difference between all flavors, for which bounds were reported by previous experiments[25], see fig. 2.5.

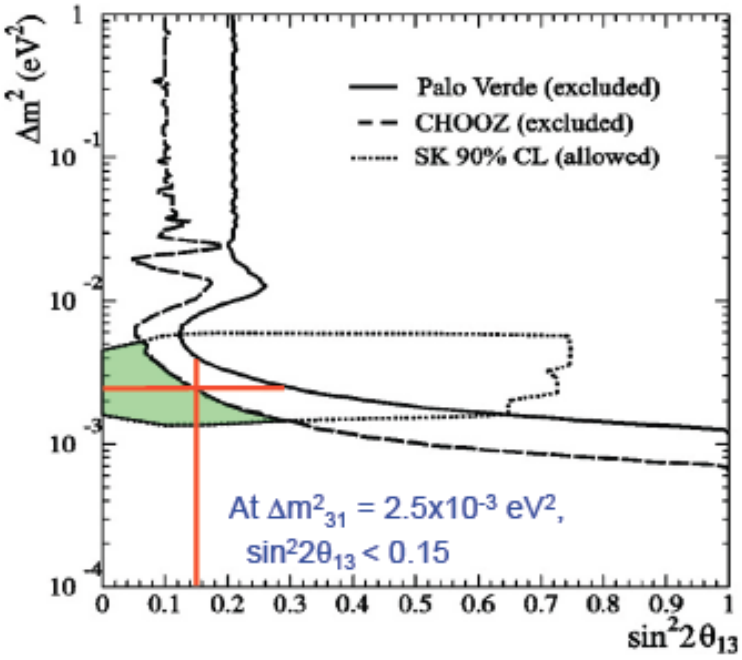


Figure 2.4: The experimental bound on $\theta_{13}$ and $\Delta m^2$[25].

Rock shielding against cosmogenic backgrounds, known as the overburden, is also a key consideration in selecting the location. Table 2.1 shows the overburden, in the unit of meters water equivalent(m.w.e.), at each site.

| | DayaBay Site(m) | LingAo Site(m) | Far Site(m) |
|---|---|---|---|
| DYB cores | 363 | 1347 | 1985 |
| LA I cores | 857 | 481 | 1618 |
| LA II cores | 1307 | 526 | 1613 |

Table 2.1: Rock overburden of each experimental site in m.w.e.

The location of each experimental site, is designed to maximally illustrate the oscillation pattern based on the electron anti-neutrino disappearance probability, which is in turn based

on the previous best knowledge of mass squared difference. A study by P.Huber et al[26], predicted the experimental sensitivity in fig. 2.5.

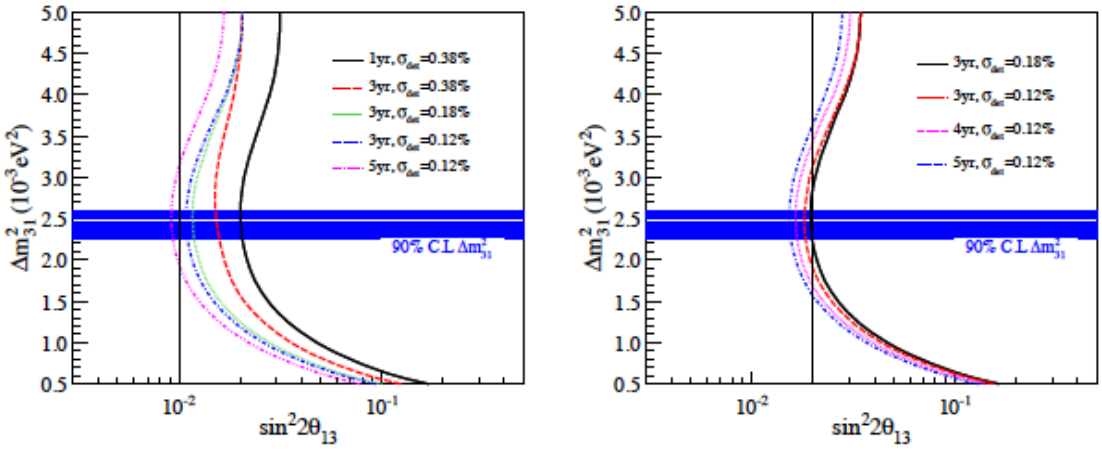


Figure 2.5: Predicted experimental bound on $\theta_{13}$ and $\Delta m^2_{31}$ by P.Huber et al. The left and right plots represented a discovery at 3 sigma and 5 sigma level with different runtime and detector systematic uncertainties[26].

The probability of an electron anti-neutrino, emitted from the reactor cores, being detected as an electron-type in the detector, is given by,

$$P_{ee} \approx 1 - \sin^2 2\theta_{13} \sin^2 \left( \frac{\Delta m^2_{31} L}{4E_\nu} \right) - \cos^4 \theta_{13} \sin^2 2\theta_{12} \sin^2 \left( \frac{\Delta m^2_{21} L}{4E_\nu} \right) \tag{2.11}$$

where $L$ is the distance travelled by the neutrinos, or the designed baseline distance in the experiment. Figures 2.6 and 2.7 show how the KamLAND and Daya Bay detectors were placed for maximum sensitivity to the mixing angles, $\theta_{12}$ and $\theta_{13}$ respectively.

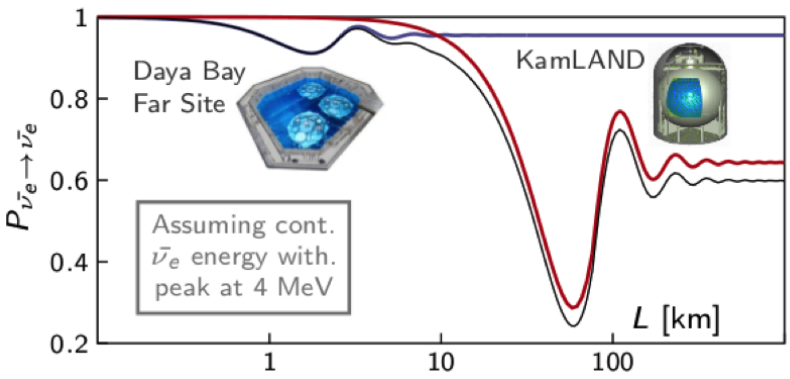


Figure 2.6: Maximal sensitivity of DYB at 1km to $\theta_{13}$ as compared to KamLAND in $\theta_{12}$

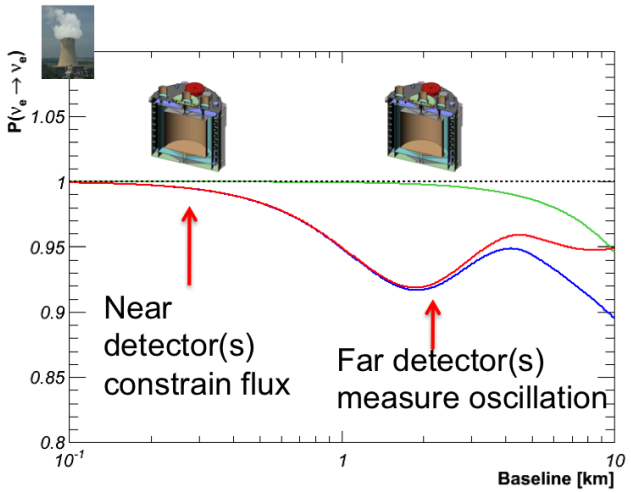


Figure 2.7: Near(Far) detector location corresponding to null(maximal) oscillation probability.

## 2.4 Anti-neutrino Detector(AD)

The Daya Bay experiment deployed a total of eight functionally identical ADs[27] at three sites. Each near site housed two ADs and the Far site housed four ADs. Each AD uses a 3-layer design, with different liquids in each concentric cylindrical tank. The AD consisted of an Inner Acrylic Vessel(IAV), an Outer Acrylic vessel(OAV) and a Stainless Steel

Tank(SST). The detector dimension is summarized in table 2.2.[28]
The IAV contains primary target for reactor electron anti-neutrinos with 20 tons of gadolinium-doped Liquid Scintillator(GdLS)[29]. The space between IAV and OAV is used as a gamma ray catcher and also as a secondary target for nH capture. It holds 20 tons of pure liquid scintillator(LS). SST is the outermost tank containing both IAV and OAV and 40 tons of mineral oil(MO). It serves as a radiation shield against natural radioactivity from surrounding rock in each site. Figure 2.8 showed the CAD drawing of the cross-sectional view of the ADs.
To detect photons generated from scintillator through the transparent AVs, 192 Photo-Multiplier Tubes(PMT) has been mounted onto 8 PMT ladders in each AD. Reflected photons are minimized by placing black panels behind the PMTs along the circumference of ladders while specular reflectors are placed at the top and bottom of the SST facing OAV to prevent photon loss through the ends of the cylinder.

| Dimension | IAV | OAV | SST |
|---|---|---|---|
| Diameter(mm) | 3100 | 3970 | 4976 |
| Height(mm) | 3100 | 3970 | 4976 |
| Wall thickness(mm) | 10 | 15 | 12 |
| Vessel Weigh(ton) | 0.6 | 1.4 | 20 |
| Liquid Weight(ton) | 20 | 20 | 40 |

Table 2.2: Dimension and weight of each tank in AD.

### 2.4.1 Detection Mechanism: The Inverse Beta Decay

The neutrino interaction cross-section on protons is very small, about $10^{-44}$ $cm^2$[30] and therefore a large proton target pool is needed to maximize detection. The detection of neutrinos involves a coincidence tagging of prompt and delayed reactions, separated by a

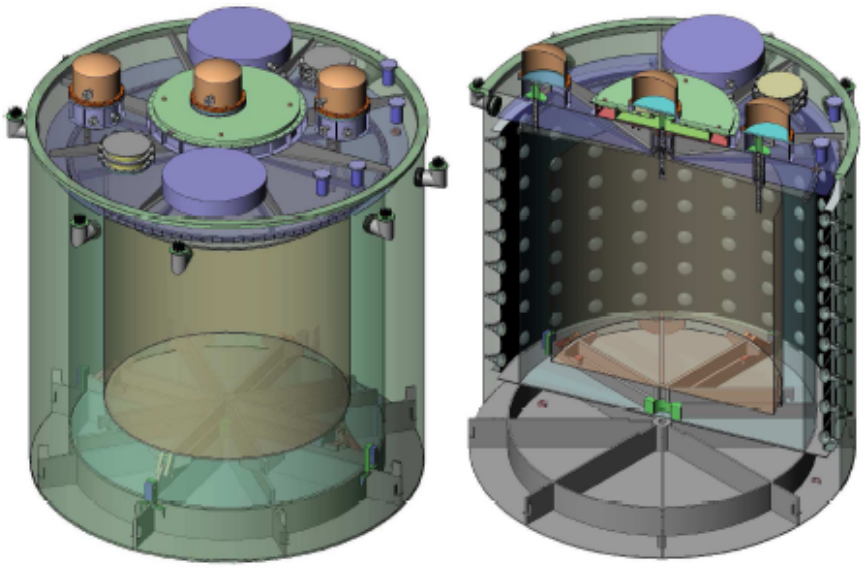

Figure 2.8: Cross-sectional view of AD, including Photo-Multiplier Tubes(circles on the black rim), and Auto Calibration Units(three cylinders on the top).

mean free time of 27 $\mu s$.

The prompt reaction is an inverse beta decay(IBD) in which a neutrino interacts with a proton producing a neutron and a positron,

$$\bar{\nu}_e + p \rightarrow e^+ + n \tag{2.12}$$

The total cross-section of this reaction, neglecting terms of order $E_\nu/M$, where $E_\nu$ is the anti-neutrino energy and M is the nucleon mass, is given by,

$$\sigma_{tot}^{(0)} = \sigma_0(f^2 + 3g^2)(E_e^{(0)} p_e^{(0)}/1MeV^2) \tag{2.13}$$

where $E_e^{(0)} = E_\nu - (M_n - M_p)$ is the positron energy when the neutron recoil energy is neglected, and $p^{(0)}$ is the positron momentum. The weak coupling constants are $f = 1$ and $g = 1.26$, and $\sigma_0$ is related to the Fermi coupling constant, $G_F$, the Cabibbo angle, $\theta_C$, and an energy-independent inner radiative correction. The IBD process has a threshold energy in the lab frame $E_\nu = [(m_n + m_e)^2 - m_p^2]/2m_p = 1.806MeV$. The signal of the prompt reaction is augmented by the positron-electron annihilation resulting in an additional 1.022

MeV gamma rays which deposit their energy in the scintillator through Compton scattering. The capture of the prompt neutron by Gd in IAV scintillator forms a delayed reaction named the nGd capture(2.14). The neutron can also be captured by a proton(hydrogen nucleus) in scintillator, either within the IAV or the OAV, named nH capture(2.15).

$$n + Gd \rightarrow Gd^{*} \rightarrow Gd + \gamma(8MeV) \tag{2.14}$$

$$n + p \rightarrow d + \gamma(2.2MeV) \tag{2.15}$$

The purpose of doping Gd into liquid scintillator is to enhance the neutron capture cross-section which is about 150,000 times higher than the nH capture. The nGd capture results in 8 MeV of gamma emission from the two isotopes of Gd, $^{155}Gd$ and $^{157}Gd$[28]. Monte Carlo predicts that, on average, about 160 photoelectron/MeV will be detected by PMTs with about $9\%/\sqrt{E}$ energy resolution in the MO region. The gamma catcher region is responsible for those gamma rays that escape from the GdLS region. Figure 2.9 shows the low energy tail in the LS region with at least one gamma ray captured.

The MO region has very little scintillation light. It is used to provide attenuation against radiation from the PMT glass as well as from the natural radiation from SST, surrounding rock and radon. It also provides enough space for PMTs to receive uniform light from photon interaction vertices within the LS.

### 2.4.2 Liquids and PMT

The GdLS, which is doped with Gd to 0.1% by mass, is chemically based on the organic solvent Linear Alkyl-Bezene(LAB). LAB has the advantage of high flash point, low volatility, high light yield and good compatibility with the detector materials[29]. The doped scintillator is mixed with two wavelength shifters(fluors) to modify the wavelength of the emitted light from GdLS from the UV region to the visible region where the PMTs have the highest sensitivity. All liquids in AD are designed to have the following properties[28].

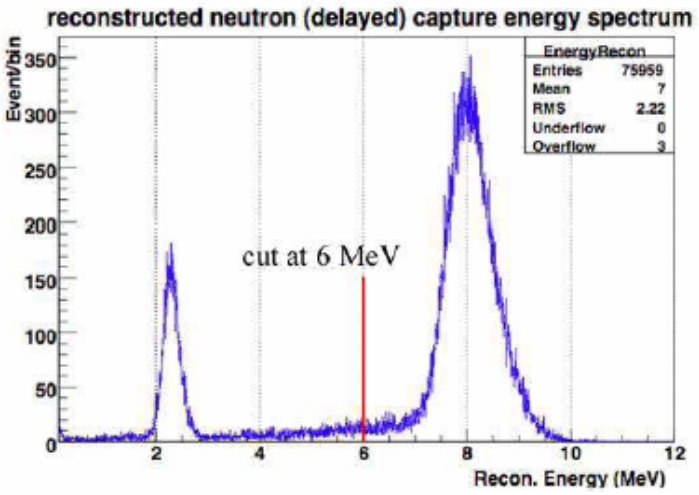


Figure 2.9: The neutron capture energy spectrum by Geant4 simulation. 8 MeV peak corresponded to nGd capture[28]

- Good chemical stability: to ensure 5 years of data-taking
- long attenuation length: to ensure good light collection and energy resolution
- High scintillation yield(except MO): to ensure high energy resolution
- High radio purity: to reduce accidental singles

The GdLS also required the additional advantages of high neutron capture cross-section, and high total capture photon energy to implement effective cut to backgrounds.

Photons generated by GdLS or LS, (figure 2.10) will eventually pass through all transparent liquids and AVs to reach the PMTs inside AD. All the PMTs are Hamamatsu R5912 with an 8-inch hemispherical, high radio-purity, Boro-silicate glass[28]. The quantum efficiency(QE), referring to the efficiency to convert incident photons into photoelectrons, of the R5912 is about 25% at 390nm and the peak cathode sensitivity is at 420nm. The overall PMT cathode coverage is about 12% of the total surface area in the AD, with the top and bottom specular reflectors. Therefore, it is critical for the GdLS to generate enough photons with wavelength matching the sensitivity of PMT to compensate for the low PMT coverage and maintain high energy resolution.

Figure 2.10 shows the GdLS under UV lamp illumination. Figure 2.11 shows the interior

of SST with PMTs mounted on ladder. Figure 2.12 shows the optical spectra of various components.

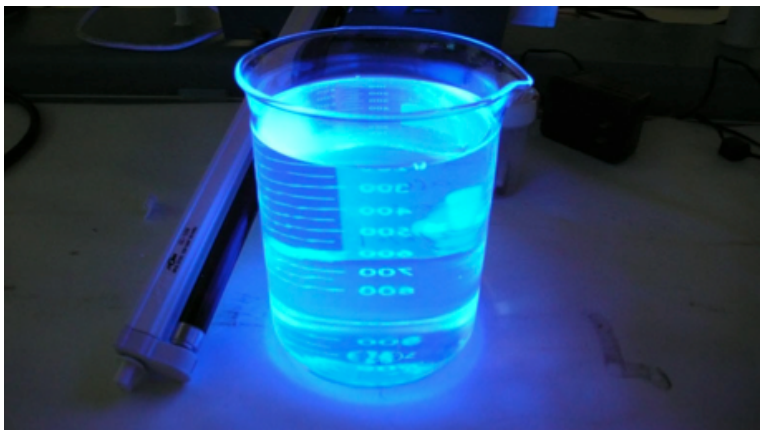

Figure 2.10: GdLS illuminated by UV lamp.

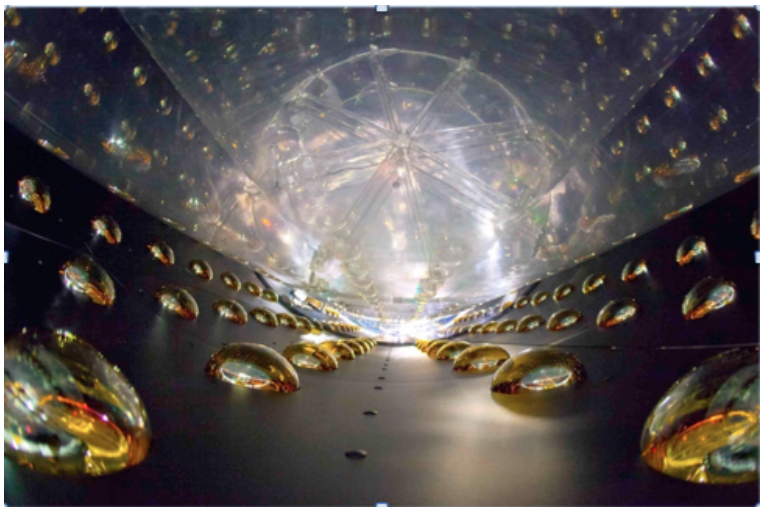

Figure 2.11: Interior of AD with 8 PMT ladders(black) with 24 PMTs each facing OAV and IAV.

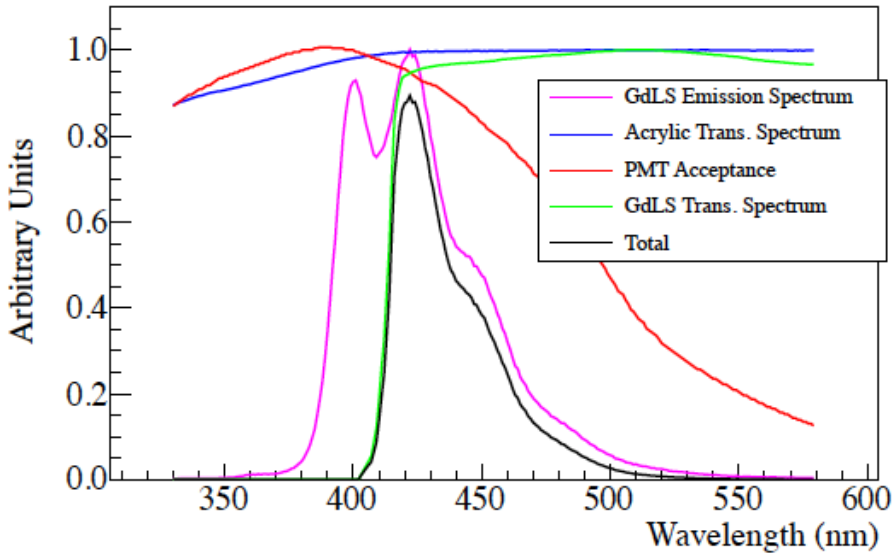


Figure 2.12: Optical spectra of photons at different stages. Specular reflectance not included as it is almost maximal in the range concerned.[28]

## 2.5 Muon Veto Water-Pool Detector

The AD is the central component of the entire detector system in the Daya Bay experiment. However, muon spallation products and natural radioactive isotopes can produce nuisance signals in the AD. Those neutrons and random singles, may occurred in temporal coincidence inside an AD, and contribute to IBD candidate which could then incorrectly affect our measurement. Therefore, a water-pool detector achieving the following goals is used.

• Tagging muons that passed close to the AD.

• Minimizing the likelihood of muon spallation neutron getting into AD without being tagged.

• Minimizing random gammas from Rn, U, K, Th etc. from surrounding rock and materials.

Studies show that 50 cm of water could reduce the flux of gammas with an energy of 1-2 MeV by a factor of 10. ADs in each site are placed minimum distance of 2.5 m away from the edge of the water-pool which reduces the singles by five orders of magnitude.

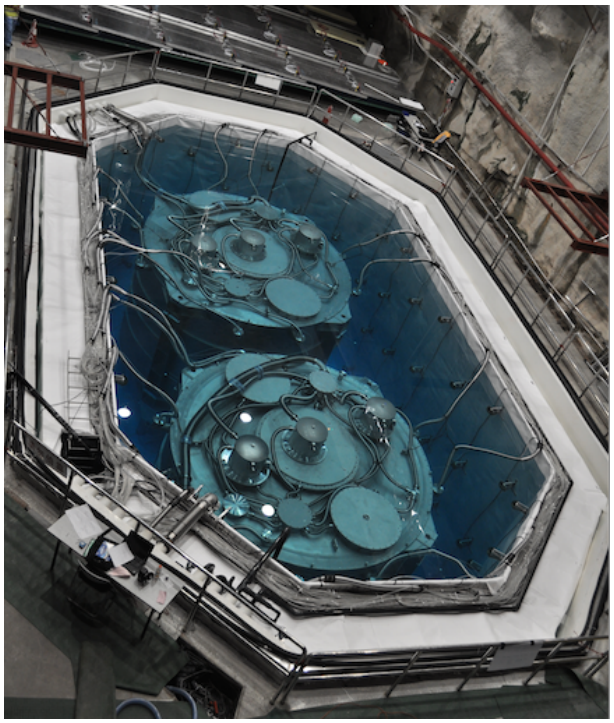

Figure 2.13: A fully deployed water-pool detectors with two ADs in EH1.

The muon veto detector implemented a two-layer octagonal design. To separate the pool into inner(IWS) and outer(OWS) water systems. At tyvek film (1070D)[31], see fig 2.14b) is stretched over a stainless steel instruct frame, see fig 2.14a. The IWS houses all ADs, either two(near) or four(far). The OWS sits 1 m outside the IWS and the bottom on all sides. The detector is 10m in depth, 16m in length and 10m(16m) in width which contained 1400 tons(2170 tons) of 18 Mega-ohm pure water in near(far site).

The water-pool PMTs in both water shields are used to detect Cherenkov light by incoming muons as a muon veto. PMTs are either 8-inch new Hamamatsu R5912 or refurbished from previous experiment MACRO[32]. The overall PMT coverage is about 0.6%. The number of PMT in three site is tabulated in table 2.3.

(a) Assembly of OWS with unistrut.

(b) Partitioning with Tyvek. PMT shown in OWS.

Figure 2.14: Muon veto detector

| | DYB Site | LA Site | Far Site |
|---|---|---|---|
| IWS PMT | 121 | 121 | 160 |
| OWS PMT | 167 | 167 | 224 |

Table 2.3: Number of PMT in each partition, each site.

### 2.5.1 Resistive Plate Chamber(RPC)

The muon veto water-pool has an efficiency of higher than 99%[33] and to further tag those missed muons, a stack of RPC sits above the water-pool. The RPC system is placed on a rolling platform which can be slid to cover the entire surface of water-pool. Figure 2.15

shows a view of the RPCs before sliding over the pool.

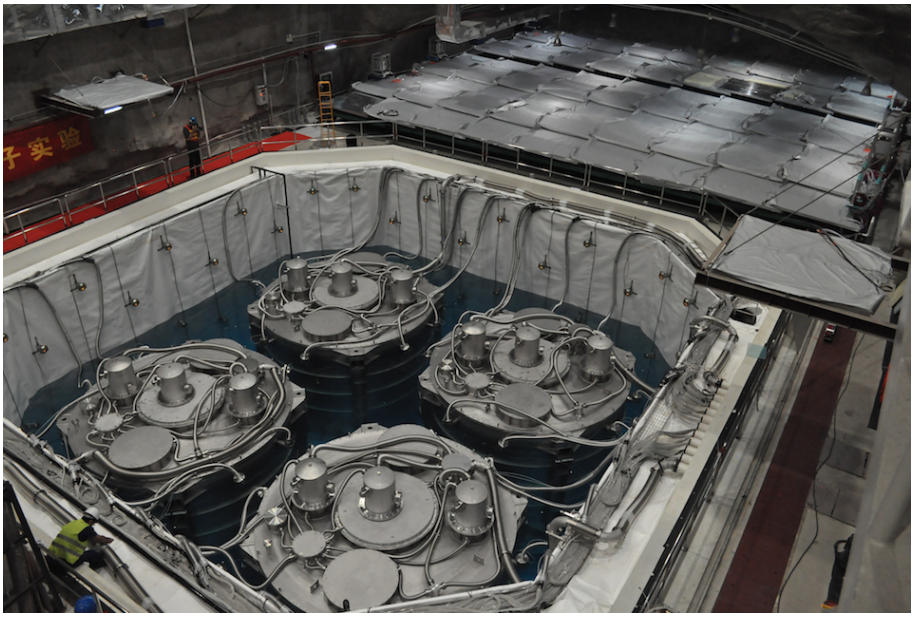

Figure 2.15: RPC array(9x9) on the top right and water-pool housing 4 ADs in the Far site.

Each module of RPC detector consisted of 4 pairs of bakelite resistive plates encased in a square aluminium box[34]. The pair of resistive plates encloses a small gap of 2 mm filled with a mixture of gas. A potential of 8000 V is applied across the gas gap. With each plate generating an electric field, ionization triggered by charged muons could be detected by the readout strips. The four pairs of RPC within a module are aligned to have readout strips covering both X and Y directions for 2D position resolution[35]. Other layers of material in the module including isolation pad and signal ground are shown in figure 2.16a.

Taking into account the incident angle of muons into the experimental site and the dead area of each RPC module. The detection efficiency using a trigger condition of 3 layers out of 4 is about 97%. Combining with the water-pool, the overall efficiency of the muon veto system very close to 100%. The number of RPC module used at each near site is 9 columns

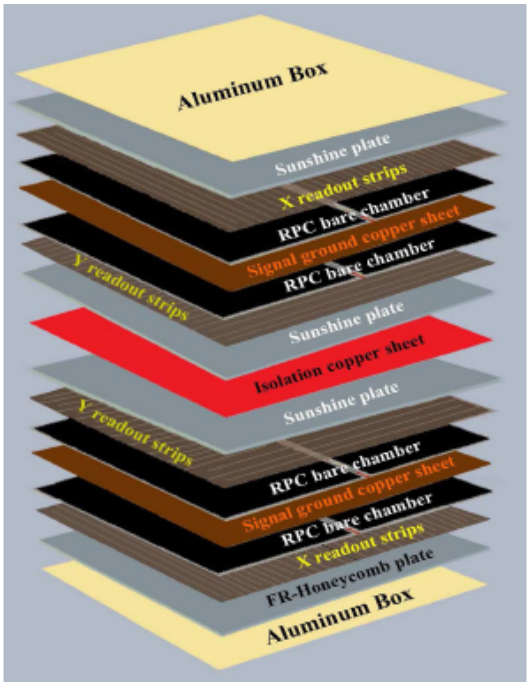


(a) Schematic of multiple layers in one RPC module.

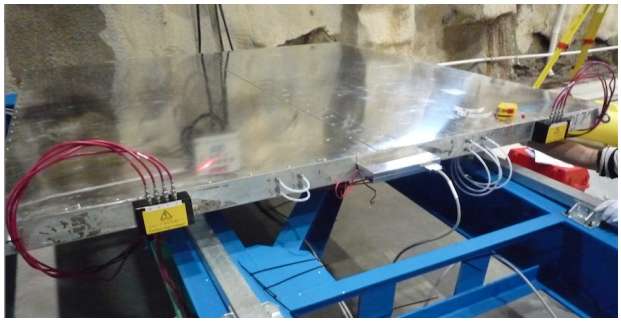

(b) One module of RPC.

Figure 2.16: RPC detector module

by 6 rows while at the Far site it is 9x9.

# Chapter 3

# Detector Calibration

## 3.1 Motivation

The three types of detectors in the Daya Bay experiment are critical to the detection of IBD events as well as suppression of backgrounds. However, those functions would not be well-performed unless each detector is sufficiently calibrated[36]. The calibration of each detector is listed below,

- Energy calibration at different positions in AD[37].
- Timing calibration of PMTs in AD and water-pool.
- Voltage gain calibration of PMTs in AD and water-pool.
- Detection efficiency calibration of RPCs[35].

The calibration of PMTs is mainly to correct timing offsets introduced by PMT electronics and the voltage gain which determines the energy resolution. The RPC calibration sets the value of high voltage applied to each plate for maximal efficiency. Energy calibration in the AD is most important for understanding the energy deposition as a function of energy so that a detector energy response model can be constructed.

## 3.2 Energy Calibration in AD

The energy calibration in AD is implemented according to the interactions of IBD. Therefore the radioactive sources used are similar in energy to IBD events. These are, a positron source, a neutron source, a gamma source and an LED at various voltages. To build the detector energy response model[38], other energy ranges obtained from natural radioactive isotopes within AD are used in addition to those mentioned sources. The radioactive isotopes responsible for each process are marked below,

| | neutron | gamma | positron |
|---|---|---|---|
| Source | $^{241}$Am-$^{12}$C | $^{60}$Co | $^{68}$Ge |
| Energy (MeV) | 7.97 | 2.48 | 0.94 |
| Rate (Hz) | 0.5 | 86.0 | 15.3 |
| Usage | neutron response, capture time, absolute & relative eff. | energy linearity, spatial & temporal variation, quenching | positron response, trigger threshold, energy scale |

Table 3.1: Radioactive sources for calibrating AD. Energy is reconstructed in AD and rates are the AD detected rates when sources are deployed.[39]

With the IBD interaction in the AD, there is a prompt reaction including the emission of a neutron and a positron, which annihilate with an electron, giving out two 511 keV gammas. The emitted neutron would then be captured, mainly by Gd but also by hydrogen giving out either 8 MeV of gammas or a single 2.2 MeV gamma. The energies reconstructed using PMT in the AD do not exactly match the expected peak energy of each source, mainly because the energy response of the liquid scintillator and the acrylic vessels are not ideal. The energy calibration, is used to construct an energy response model intended to correct the reconstructed energy for these effects.

An americanium-carbon and cobalt sources are combined in a single capsule while the germanium is encapsulated alone. Each set of sources is then parked in an Automated Calibration Unit(ACU)[40], which is located on the top of the AD lid. There are three ACUs on each AD that perform calibrations in the GdLS central axis, the GdLS offset axis and the LS respectively. Figure 3.3 shows the measured spectrum of AmC, Co and Ge in AD.

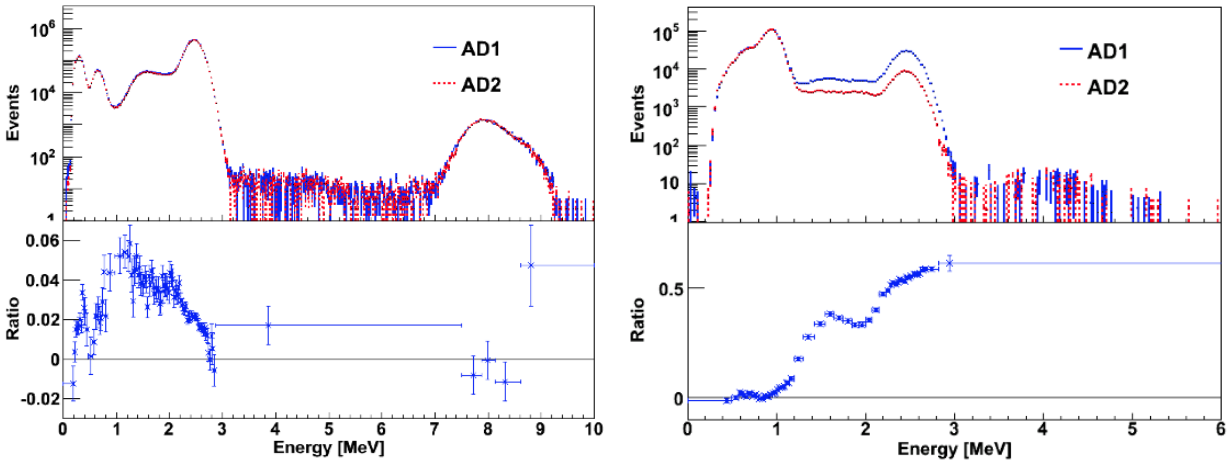


(a) AmC and Co measurement.

(b) Ge measurement.

Figure 3.1: ACU source measurements. The 2.5 MeV peak is the gamma emission from Co and the 8 MeV is the n-Gd gamma emission from AmC. The ratio is the difference between AD1 and AD2.[39]

These ACU sources are deployed in the AD on a weekly basis for offline monitoring of the AD response. To build the detector energy response model, additional calibration sources were used during the summer shutdown in 2012. In addition, some naturally occurring radioactivity inside AD is used. Figure 3.2 lists the sources used in the summer calibration. The energy resolution of the AD at different energies is plotted using the sources. The fitted resolution using the BNL-Caltech-William and Mary (BCW)[39] construction, is found to be,

$$\frac{\sigma_E}{E} = 1.16\sqrt{(1.13\%)^2 + (\frac{7.9\%}{\sqrt{E}})^2 + (\frac{5.1\%}{E})^2} \tag{3.1}$$

where the first bracket represents the spatial-temporal resolution. The second one is due to photon statistics and the third is from constant noise[38]. Figure 3.3a shows the resolution versus energy.

| Sources | $E_{true}$ [MeV] | $E_{rec}$ [MeV] |
|---|---|---|
| $^{137}$Cs | 0.662 | 0.632 |
| $^{54}$Mn | 0.835 | 0.818 |
| $^{68}$Ge | $0.511 \times 2$ | 0.934 |
| $^{40}$K | 1.461 | 1.469 |
| n$^{1}$H (PuC) | 2.223 | 2.287 |
| n$^{1}$H (AmBe) | 2.223 | 2.291 |
| $^{60}$Co | 1.173 + 1.333 | 2.453 |
| $^{208}$Tl | 2.615 | 2.710 |
| $^{12}$C* (PuC) | 4.439 | 4.769 |
| $^{12}$C* (AmBe) | 4.439 | 4.982 |
| n$^{12}$C (PuC) | 4.945 | 5.114 |
| n$^{12}$C (AmBe) | 4.945 | 5.117 |
| $^{56}$Fe* | 5.970 | 6.07 |
| $^{16}$O* | 6.129 | 6.342 |
| n$^{56}$Fe | 7.630 | 7.842 |
| nGd (IBD) | $\sum = 8.047$ | 8.026 |

Figure 3.2: List of sources used to calibrate the AD. K, Tl, Fe and O are naturally occurring radioactive isotopes in the AD.[38]

The energy response model, also called Non-Linearity(NL) model[41], is determined for gammas, positrons and electrons to correct for the non-linear response introduced by the AVs, scintillator and electronics. Disparity between the AD detected peaks to the well-known peaks from sources is fitted to an universal curve for each particle type, in various energy ranges from 0.5 to 10 MeV. Constraints to the model also come from bismuths and muon spallation products such as boron with continuous spectra over energy. Figure 3.3b shows the ratio of true energy to AD reconstructed energy and figure 3.4 shows the AD energy response model for each type using BCW construction. The final non-linearity model is a combined fit of the 5 models from several analysis groups.

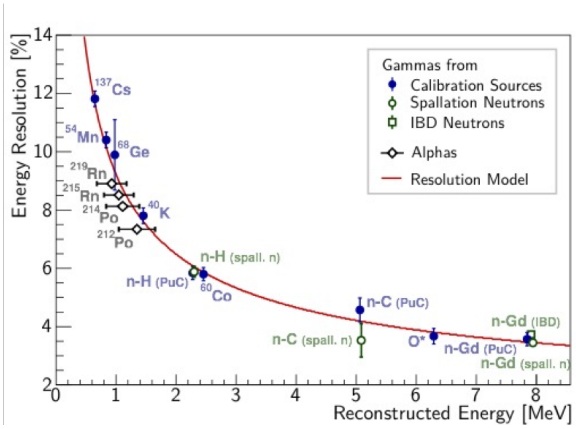


(a) Fitted energy resolution over different sources at various energies.[42]

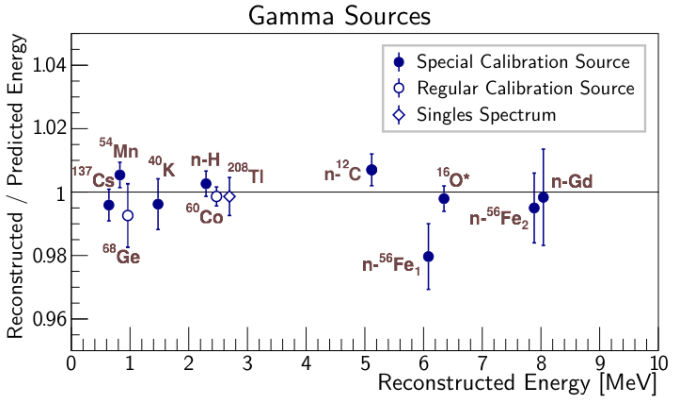


(b) Ratio from gamma peak to build NL.

Figure 3.3: Radioactive sources employed in AD for resolution and energy model.

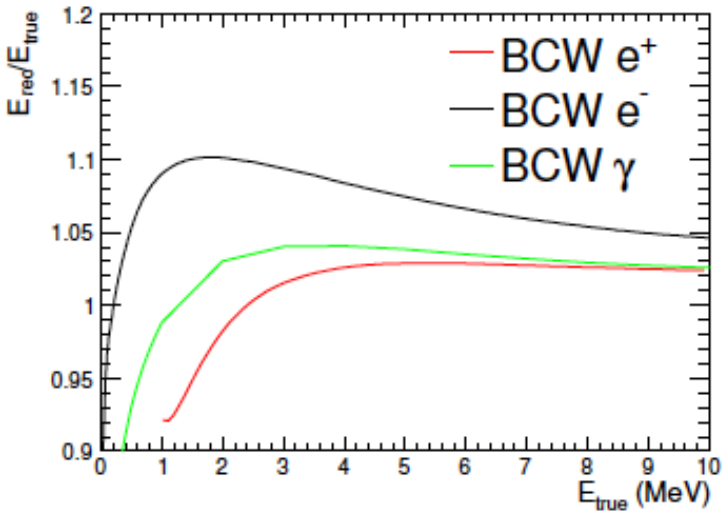


Figure 3.4: BCW energy response model for electron, positron and gamma in AD.[38]

## 3.3 PMT Calibration in AD and WP

The calibrations of PMTs in AD and WP involve the determination of timing offsets in PMTs receiving photons, as well as the tuning of the high voltage to obtain a common voltage gain among all PMTs. The two calibrations are achieved per-channel using a fixed light

source of Light Emitting Diode(LED) together at known trigger time.

The timing offset of a PMT refers to the relative offset of that PMT to other PMTs in the WP, or an absolute offset in the AD, due to different PMT configurations. In the WP, the timing of PMTs is a sum of the time of flight, PMT dynode electronics, PMT cable transmission and Front-End Electronics(FEE). The difference of this total time, among PMTs, are then assigned to be the time offset. The offsets in WP are introduced, in part, because two different types of PMTs are used, Hamamatsu and Macro, for which there are different timing in photon response and dynode electronics. For the PMTs in AD, the offset is the total time taken from light source trigger to FEE signal, subtracted by all individual timings listed above. Figure 3.5 shows the results of the relative time offset in the WP.

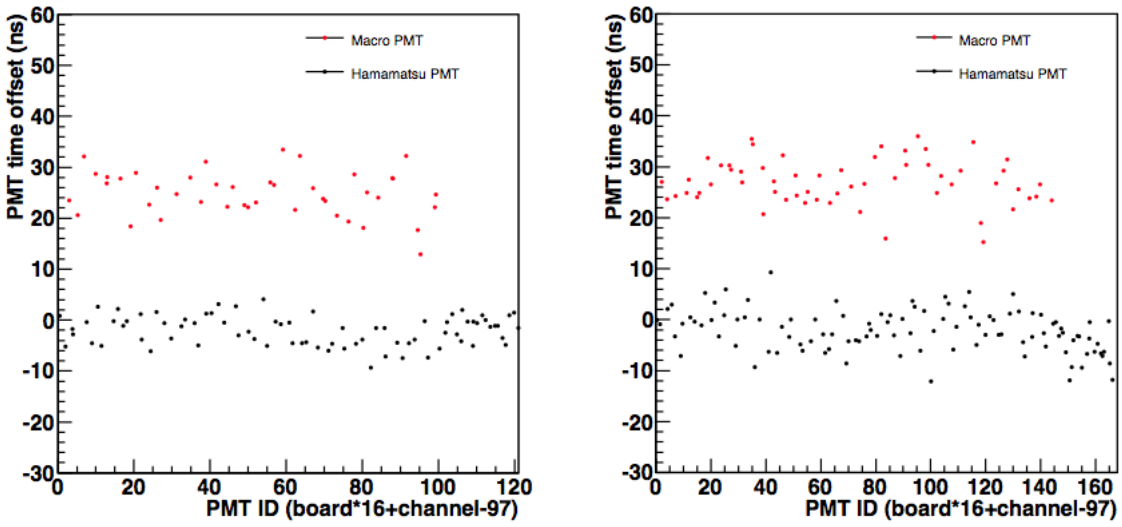


Figure 3.5: Relative PMT time offsets in WPO(right) and WPI(left). A clear distinction between Hamamatsu and Macro tubes.[43]

For monitoring voltage gain, an isotropic and homogeneous LED source would give each PMT approximately same number of photons, which would convert to photo-electrons(pe) and the FEE signal. By checking the average charge obtained by the majority of PMTs and looking for outliers, either too low or too high, one could then tune the high voltage of the

PMT to recover the nominal gain. The gain of each PMT is pre-determined by the single photo-electron calibration done before the PMTs were installed.

### 3.3.1 LED in WP

The light source used in WP and AD are the same, but the deployments are different. The LED is pulsed by a thumb-nail sized electronic circuit board(driver card) which is powered and controlled by a microprocessor through a control board. The control board, capable of pulsing 30 channels, couples a TTL signal and a DC voltage through the transmission cable to the driver board and provides time stamp to the experiments Data Acquisition (DAQ) system. Each near site WP has 50 LEDs and the Far site has 72. The LED unit consists of an LED with a peak wavelength of 430nm and a driver card, both contained in a water-sealed and transparent acrylic tube topped with a Teflon diffuser ball. This unit is mounted on a unistrut frame in the WP, 32 in the outer WP and 18 in the inner WP. Figure 3.6 shows the top-view of the LED positions.

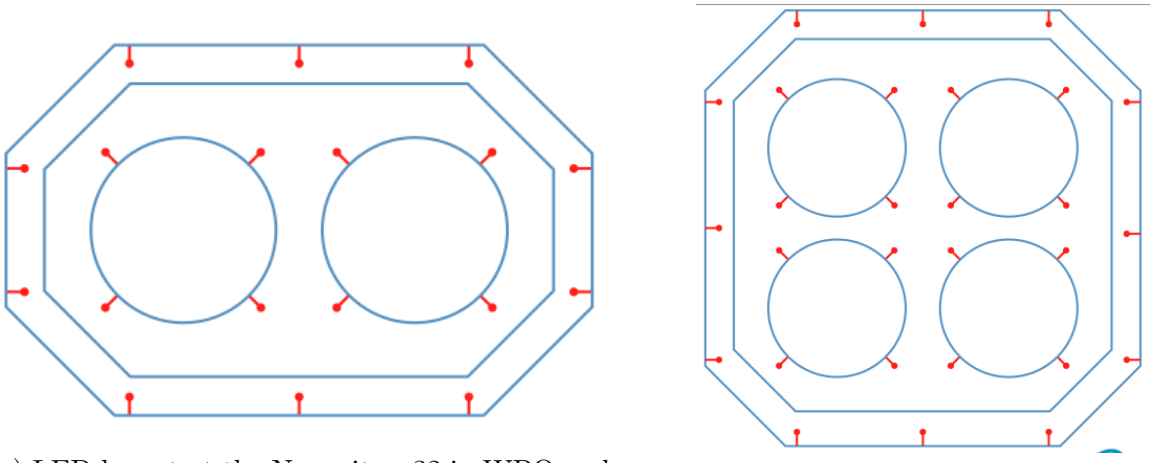

(a) LED layout at the Near sites, 32 in WPO and 18 in WPI.

(b) LED layout in Far sites, 40 in WPO and 32 in WPI.

Figure 3.6: LED layout at the Near and Far sites.

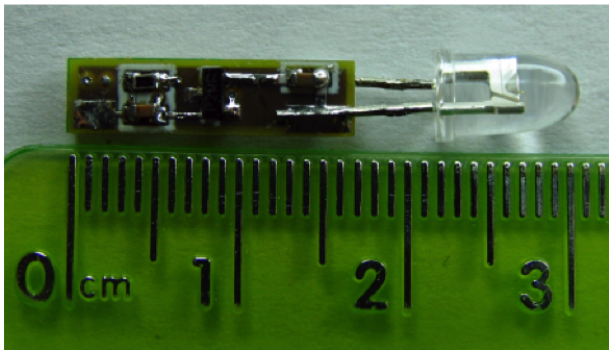


Figure 3.7: Pulser card electronics with LED.

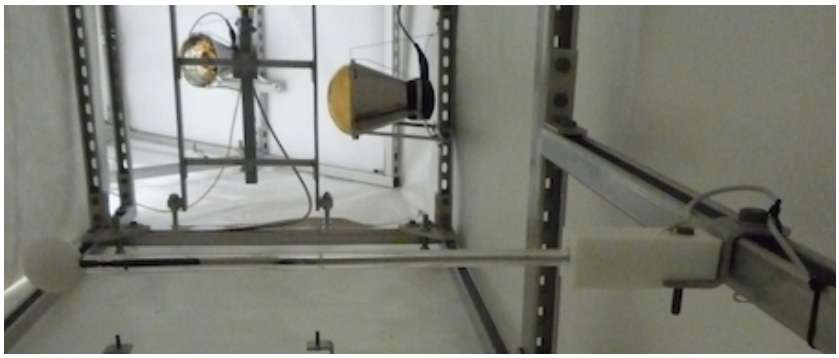

Figure 3.8: A LED unit in WP. Teflon ball, acrylic tube and black epoxy.

The driver card circuit was devised at LBNL, and miniaturized to be embedded in the diffuser ball at VT. It is directly connected to the electrodes of LED by soldering, see figure 3.7. The back side of the card is connected to a coaxial cable fastened along unistrut to the top of WP. The LED is then enclosed in spherical teflon ball attached to an acrylic tube. The driver card and LED are sealed by black 3M scotchcast epoxy. The compatibility with ultra-pure water has been tested by BNL after long-term immersion of the epoxy in water, shown in figure 3.9.

The physical requirements of the LED for PMT calibration are as follow,

• Direct light from LEDs should be able to cover all PMTs in the inner and outer WPs.

The partition between WPO and WPI is the diffuse reflective tyvek and the stainless steel frame supporting PMTs and LED as well as AD and associated pipelines could introduce

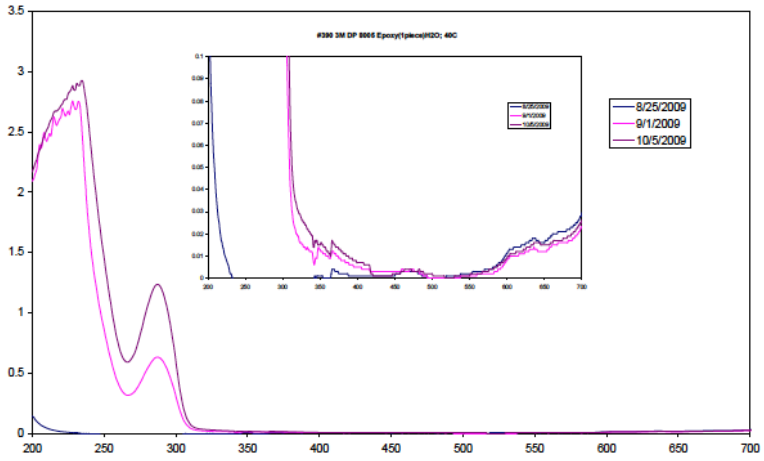


Figure 3.9: UV absorption spectrum of the water after long-term exposure to epoxy.

a lot of reflected light. Those stray light bouncing inside the pool would eventually hit PMTs which cannot be used to calibrate PMT because of the lack of accurate time of flight information. Therefore, only light from LED hitting PMT along a straight line without reflection can be used for calibration. Table 2.3 shows the number of PMTs in each WP in each site. The layout of LED deployment is that each LED being able to directly hit several PMTs while each PMT would be able to be hit by more than one LEDs. Figure 3.10 shows the analyzed data of the LED-PMT position configuration.

• Light output should be isotropic and uniform from the diffuser ball

The sparse distribution of PMTs leads to different solid angles for each LED-PMT pair, and the forward facing LED cap could only emit light within a narrow angle. To fulfill requirement one, a scattering object is needed to spread out the light as isotropically and uniformly as possible. The Teflon ball used in the setup has the advantage of universal material compatibility as well as a light scattering device. A laboratory test has been done with the teflon ball to measure light isotropy. The testing setup shown in figure 3.11. The actual number of photon received by PMTs in the WP also depended on water attenuation and distance.

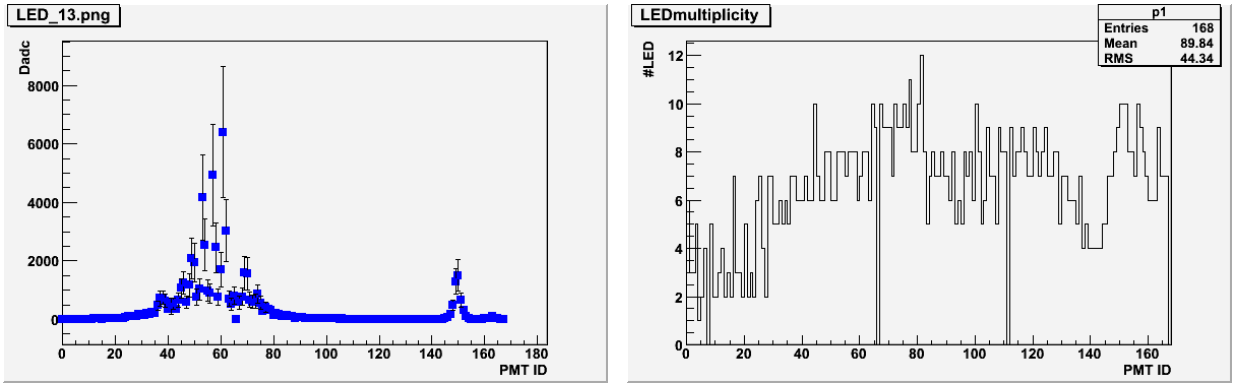


(a) More than 10 PMTs illuminated by one LED. (b) Number of LED seen by each PMT.

Figure 3.10: LED-PMT multiplicity.

$$N = N_o \Omega(d) \frac{\exp(-d/\lambda)}{d^2} \tag{3.2}$$

where $N_o$, is the number of photon emitted from LED. $\Omega$ is the geometric solid angle from LED to PMT. $\lambda$ is the water attenuation length and $d$ is the LED-to-PMT distance.

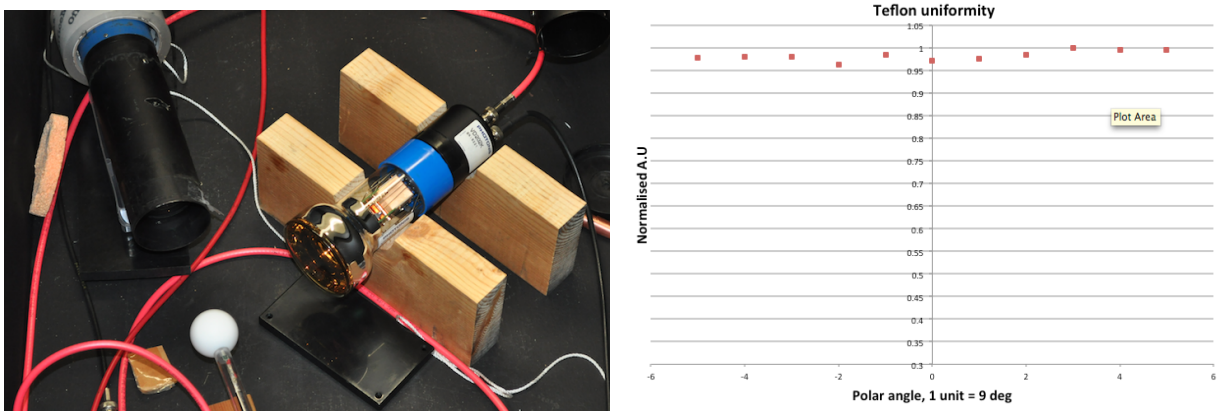


(a) Teflon ball measurement in dark box with two PMTs. (b) Measurement at various angles.

Figure 3.11: Diffuser ball uniformity measurement.

• The peak output spectrum should be around the peak sensitivity of PMT.

Similar to photon propagation from IAV to PMT in AD, the overall spectrum observed by PMT in WP is a convolution of the LED emission, teflon transmission, water transmission and PMT sensitivity. Ultra-pure water is known to have lowest absorption at around 420 nm and teflon has an over 90% transmission rate across in the entire visible spectrum[44]. Therefore, the LED emission spectrum could match PMT sensitivity closely. Figure 3.13 shows the measured spectrum of the LED in a laboratory setting.

• The pulsed light should be short in duration.

The duration of emitted light from the LED is controlled by the connected pulser card. The length of each pulse is about 3 nanosecond (ns) at the Full Width at Half Maximum(fig 3.12) so that a timing cut, TDC in the DAQ, could be implemented to select direct light in the PMT readout. Light from longer pulse is also likely to adversely affect the accuracy of the timing trigger from the LED control board to the DAQ in calibrating the PMT timing.

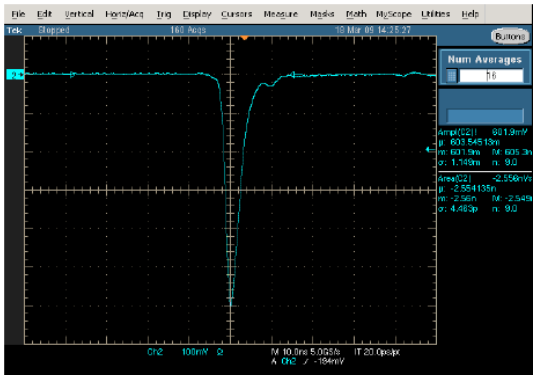


(a) Short pulse from pulser card. Steiner and Przybylski

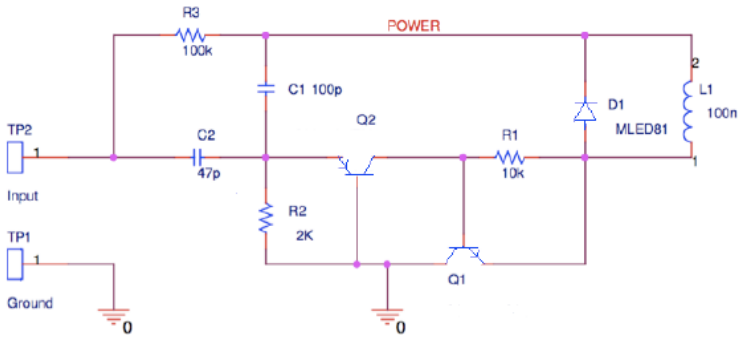


(b) Circuit diagram of the pulser card.

Figure 3.12: Pulse driving the LED and design of the card.

### 3.3.2 The MuCal Control System

This control system is responsible for channel-by-channel control of the DC voltage and a TTL pulse to each LED. The system consists of a DC power supply, a microprocessor and

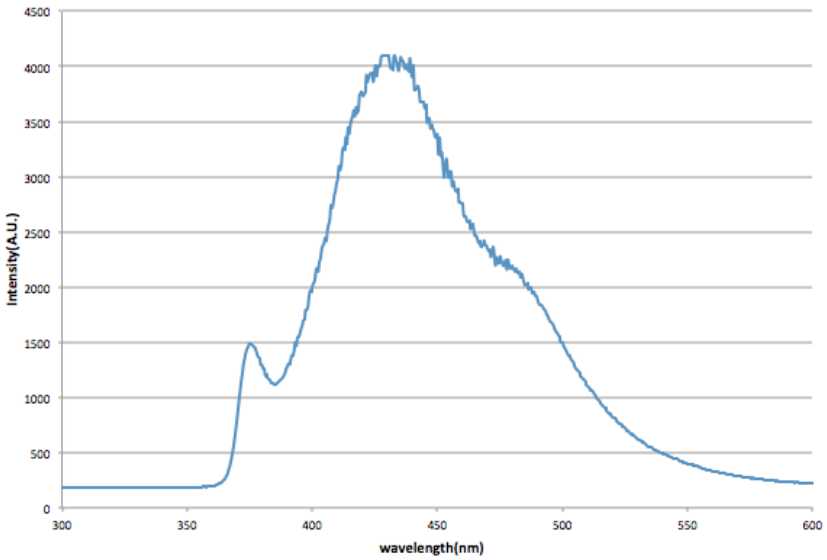


Figure 3.13: LED emission spectrum measured by CCD.

a PCB control board. Each channel of the control board has a parallel connection to a capacitor and a diode. The capacitor serves as protection to the circuit from the back flow of current downstream and a TTL signal passing through the diode coupled with a negative DC voltage to LEDs in the pool(figure 3.14). Cable impedance and attenuation were resolved by careful selection of 50 Ω termination leaving sufficient amplitude of the coupled signal.

The other function of the microprocessor and the control board is to send two synchronized signals, one PMT-like and one external trigger to the DAQ system serving as timing reference to PMT readout trigger. The PMT-like reference goes through a length of cable equivalent to the cable length from the control board to LED and WP PMTs to readout and marks the instance the LED lit up. The channel making this PMT-like signal is a serial connection of capacitor and diode for which the capacitor picks the two edges of a TTL square pulse and the diode filters out the positive polarity edge. A reduction of noise is achieved by a resistor connected to the capacitor so that only the high frequency signal can go through. The purpose of external trigger is to signal the DAQ to open a PMT readout time window so that the LED triggered PMT signal could be recorded.

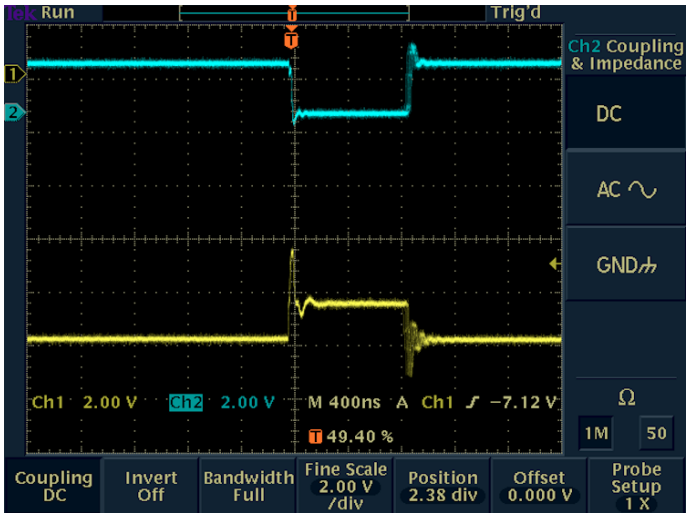


Figure 3.14: TTL signal coupled with negative DC to drive LED

The power supply of the system has a USB connection to a desktop computer in the electronics room which allows remote control of the system through a Graphic User Interface(GUI). Either automated or manual operation of all LED units at each site could be controlled using the GUI. This WP calibration has been routinely executed every week since the start of data taking of the experiment. A mini-dryrun had been done during the WP commissioning to ensure the calibration system is fully functional[45].

## 3.4 Calibration of the RPCs

The physics principle of the RPC is the ionization of the mixed gas in the chamber by charged muons and the drift of electrons along the path to electrodes. This process reaches equilibrium when the applied voltage exceeds certain value. The detection efficiency of an RPC is therefore a function of applied voltage and the plateau of the curve indicates the optimized voltage that should be applied. Raising the voltage would also lead to higher rate of noise and in retrospect lower the efficiency. The RPC modules at each experimental site are calibrated using incoming muons. A much lower rate of muons, compared with near site, in

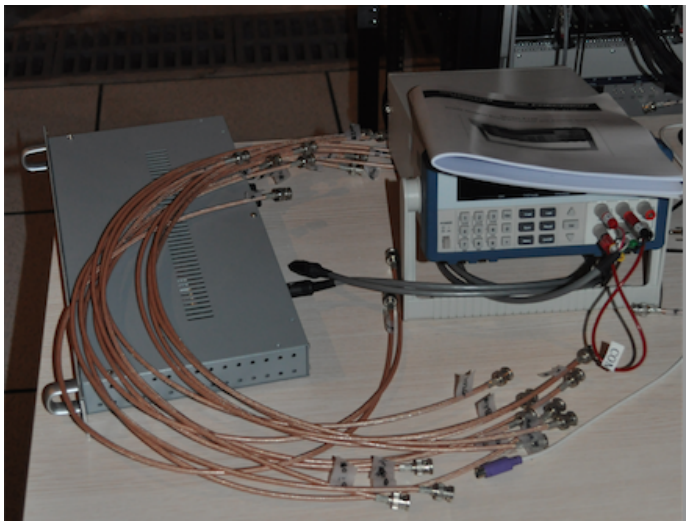

Figure 3.15: DC power supply and the controlling electronics in aluminum case.

the Far site required a different testing configuration. The real time triggering in the RPCs adopted a 2-out-of-4 selection to tag as much muon as possible while the offline analysis employed the 3-out-of-4 for a more secure selection. The 3-out-of-4 detection efficiency, for example, is calculated as follow,

$$\epsilon_{3/4} = \Pi_{i=1}^{4}\epsilon_i + \Sigma_{i=1}^{4}(1-\epsilon_i)\Pi_{j=1,j\neq i}^{4}\epsilon_j \quad (3.3)$$

$$\epsilon_i = \frac{N_{4-fold}}{N_{3-fold}} \quad (3.4)$$

where $\epsilon$ is the detection efficiency and $N$ is the detected muon rate. Figure 3.16 illustrates the difference between sites.

It is clear that High Voltage(HV) to RPC module plays a critical role in operation and it is therefore important to maintain a reliable system of HV in the experiment.

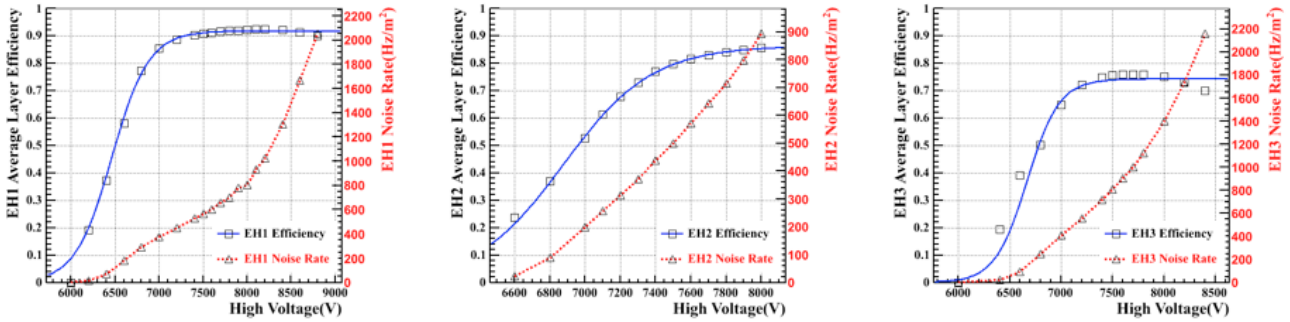


Figure 3.16: RPC detection efficiency and noise rate versus high voltage. Different efficiencies in EHs is due to different testing configurations.[46]

### 3.4.1 The RPC HV Distribution System

The HV system consists of a power supply unit, the fanout units, the RPC interface units and all the intermediate cabling.

The power supply of the HV is generated from CAEN high voltage common ground board(HV card) A1733N and A1732P together with the HV mainframe CAEN SY1527LC. The A1733N is responsible for the negative voltage of 4kV while the A1733P is for positive 6kV when plugged into the mainframe, see figure 3.17. The two near sites have one such power supply unit with two pairs of card in a climate-controlled electronics room connected with clean(low noise) power and the Far site houses three pairs. Each card has 12 output channels connected through HV cable to 12 fanout units, each of those provides nine identical outputs, for the RPC interfacing boxes on each of nine RPC modules.

All fanouts are mounted in standard racks on the RPC sliding platform. A fanout is a device with one input from the power supply and is diverted into nine output along a copper wire sprayed with HV isolation conformal coating to prevent current discharge due to unstable humidity underground (fig 3.18). The nine outputs from one fanout unit are connected to one channel of nine RPC Interface box (RPCI) on nine RPC modules responsible for powering

Figure 3.17: RPC High Voltage power supply with positive and negative HV boards.

one electrode of a layer in a module. This design, as compared with powering all the same electrodes in two modules, could avoid a total loss of functionality when the channel on a HV card died since the RPC detection employed a 3-out-of-4 triggering.

There are 2 RPCI boxes on each RPC module, one for each polarity of electrode in each layer (fig 3.21). The RPCI takes HV input from the fanouts and deliver to RPC electrodes through a filtering circuit designed to block back-feeding current to the HV power supply. The circuit is also coated against accidental discharge.

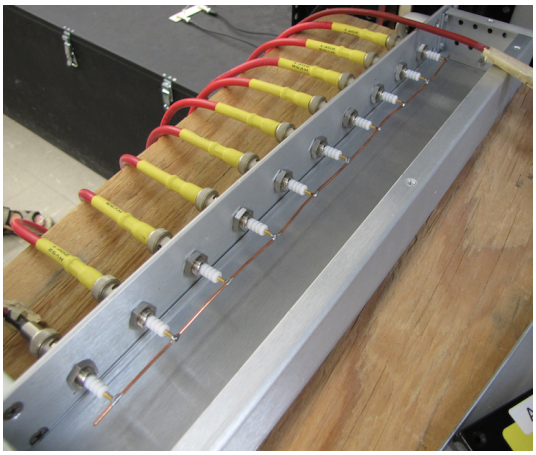

(a) Inside view of fanout.

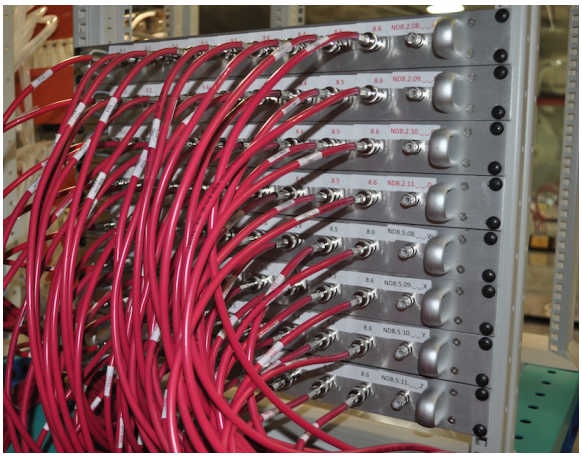

(b) Fanouts in a rack. Rightmost slots are for HV input.

Figure 3.18: Pictures of HV fanout.

(a) Inside view of RPCI.

(b) Mounting RPCI onto RPC module.

Figure 3.19: Pictures of RPCI

### 3.4.2 RPC Commissioning

The commissioning of the RPC system is not only a test to the HV sub-system, as summarized in figure 3.20, but also of the other sub-systems such as the gas supply, trigger electronics, data control system and the RPC module performance[46].

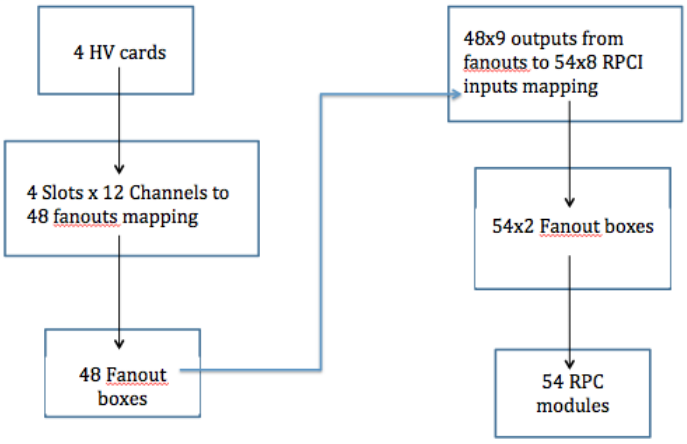


Figure 3.20: RPC High Voltage system block diagram

The most frequent issue of the system was the sparking between the RPC layers inside a module, which would lead to a abrupt rise in current drawn from the power supply resulting in a trip in that particular channel in the HV board. Total current drawn by each fanout was recorded using the readout of power supply and the distribution is plotted in figure 3.22a.The plot shows a grouping of eight fanouts supplying HV to four layers of the same nine RPC modules. The current drawn by each layer of a chamber is very sensitive to changes in temperature and relative humidity in the experimental hall. Several environmental sensors have been installed in the hall to monitor these changes. Early studies have indicated correlation between the current drawn, the temperature and humidity in the hall. Figure 3.22 illustrates such dependence using temperature sensor readings in continuous temporal sequence.

Sparks in fanouts were observed and fixed by re-coating onsite. A gas-HV interlock in the user interface has been implemented to cut off HV to the RPCs when the gas runs out. Other sub-systems have also been commissioned and different issues were reported and fixed[46].

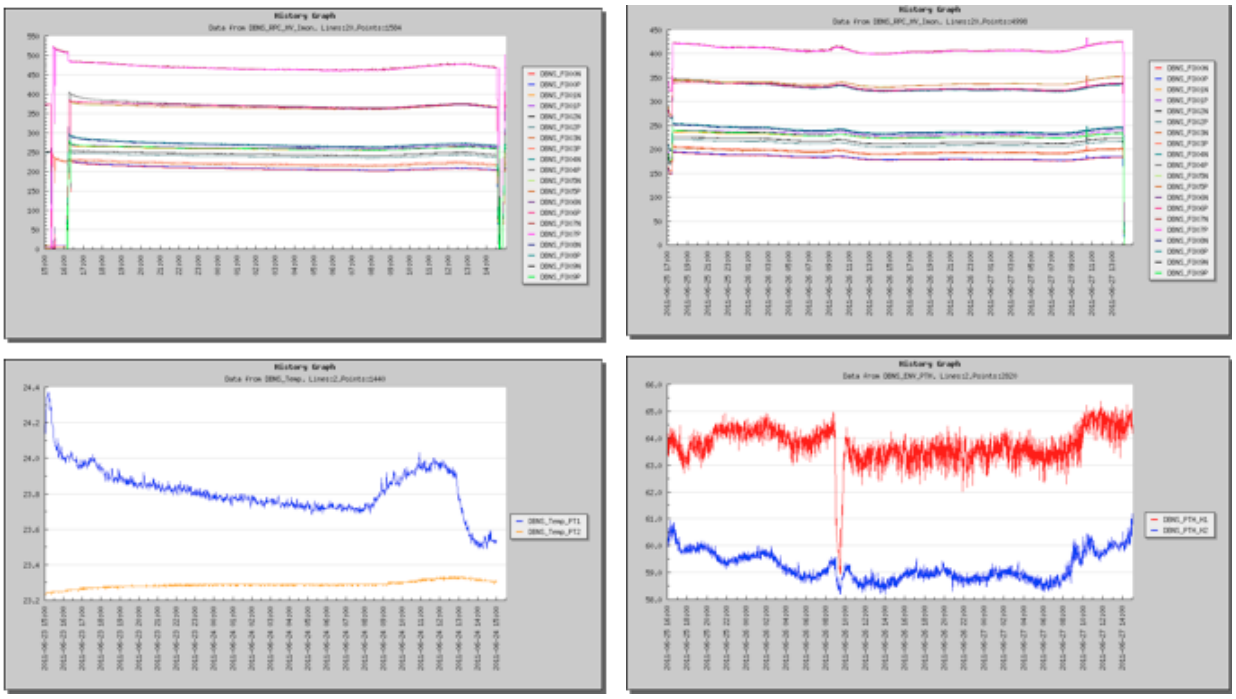

(a) Temperature dependence.

(b) Humidity dependence.

Figure 3.21: Correlation trend of RPC current drawn with temperature and humidity

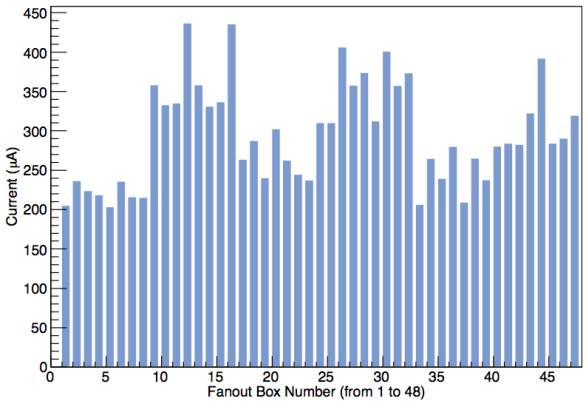


(a) Statistics of current drawn in fanouts.

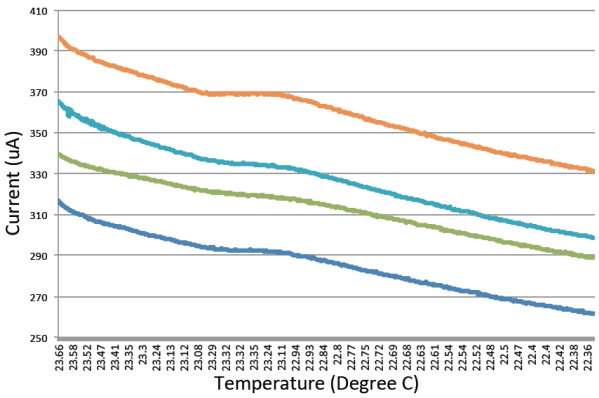


(b) Indication of temperature dependence on current drawn in RPC modules .

Figure 3.22: HV commissioning of RPC

# Chapter 4

# Water Attenuation Length Analysis

This chapter described the details of the analysis I have done on the water attenuation using LEDs, nuclear spent fuel neutrinos and the generic anti-neutrino spectrum from the Daya Bay measurement.

## 4.1 Analysis of WP LED

In addition to monitoring PMT voltage gain and timing the PMT response in the WP, one critical intention of using the LED data is to monitor changes in the water attenuation length of the pool. The WP has a circulation system to maintain the high resistivity of water, which is equivalent to maintaining long attenuation length. Attenuation is a physical process of light absorption and scattering in the propagation of light from its source to the PMTs. There is no way to distinguish between absorption and scattering in this experiment and therefore we assigned the definition of attenuation to be,

$$I = I_o \exp(\frac{-d}{\lambda}) \tag{4.1}$$

where $I_o$, $\lambda$, $d$ are the initial light intensity, the attenuation length as a function of wavelength and the distance from LED to PMT. In general, the attenuation and the initial intensity

are a function of wavelength as absorption in water depends on the frequency of radiation and the difference could be as much as 100 times. The LED emission spectrum was chosen to peak at 430 nm where absorption by water is minimized and PMT cathode sensitivity is maximized.

Major issues of the analysis are that reflected light is difficult to completely remove due to multiple reflections from tyvek and other structures in the pool and also the fact that the attenuation in water is very long because of constant water circulation in the system. Most LED-PMT pairs being too close together, are not capable of measuring the effect of attenuation and the intensity from LED to PMT could be too strong to be linear in the readouts. The strategy is to pick LED-PMT pairs which are separated as far as possible and to impose a timing cut on those PMT readouts according to the expected time of flight from the LEDs. As shown in equation 3.2, the analysis required handles on the initial intensity of LEDs and the solid angles to particular PMTs which are not known in the experiment. A relative measurement could tackle these unknowns by comparing the same pairs using different pool calibration runs to determine the relative change in the attenuation coefficients in the two runs from different weeks.

The advantage of the relative measurement is that it can monitor the change in the LED intensity in addition to the change in attenuation. Suppose $R$ is the ratio of the received intensity of a PMT from an LED of one run to another, then the relation of $R$ to distances of PMTs from the same LED is given by,

$$ln(R) = ln(\frac{I_o}{I'_o}) + d(\frac{1}{\lambda'} - \frac{1}{\lambda}) \tag{4.2}$$

The prime notation denotes the same quantities from another run. It is natural to assume different values of LED intensity and attenuation coefficient in different runs. The slope of the plot would indicate the changes of water clarity and the intercept indicates the stability of LED intensity. Figure 4.1 shows the plot of an LED with PMTs that pass the selections. The data selection for this analysis involves the selection of LED calibration data, followed by raw PMT data treatment. The external trigger from the MuCal system bus is labelled by the DAQ electronics a specific flag, called the trigger number. This number signals the

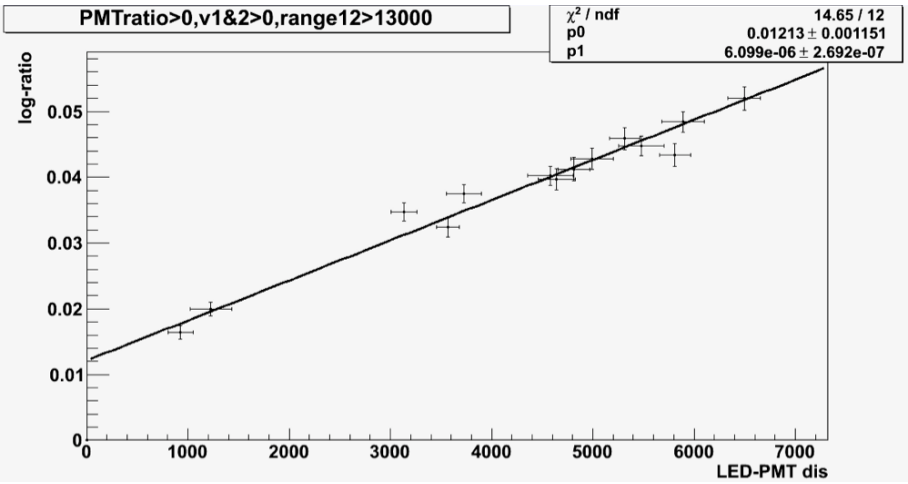


Figure 4.1: An LED-PMT plot representing a relative attenuation measurement. The LED-PMT distance is measured in mm and the y-intercept in this plot indicated 1.2% difference in the LED initial intensity between two runs with 9% uncertainty from the fit. The slope of the plot refers to the difference between the inverse of attenuation lengths of two runs.

operation of an LED in the WP and is different from other triggers such as PMT multiplicity, energy sum, random trigger and AD calibration, as shown in figure 4.2.

PMT are selected by specifying the FEE slots and channels using a known mapping. TDC and ADC cuts are then imposed to reject backgrounds due to accidental singles and muon Cherenkov light. The flasher cut has been imposed to AD PMTs but not WP PMTs because muon Cherenkov events are signaled by a high PMT multiplicity(>12) or a high energy sum which are both robust against flasher PMTs. Details of the flasher cut will be discussed later. The arrival time and magnitude of PMT signal are characterized by the TDC and ADC values.

The ADC records the total charge multiplied by the PMT dynodes governed by the voltage gain. The parameter converting the ADC value back to photoelectrons(p.e.) is determined

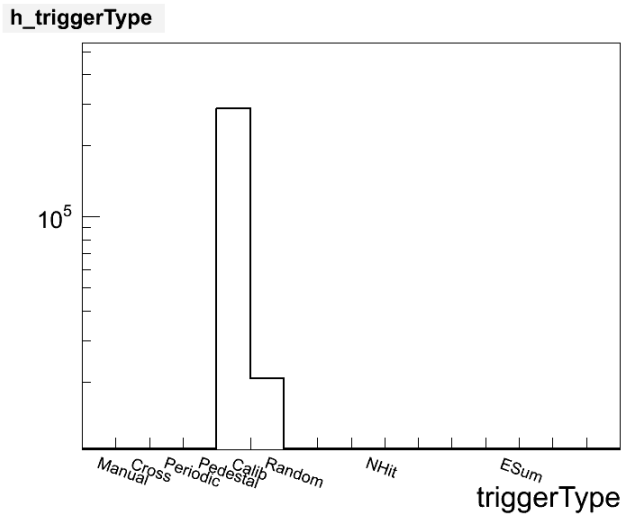


Figure 4.2: Trigger type recorded during WP calibration.

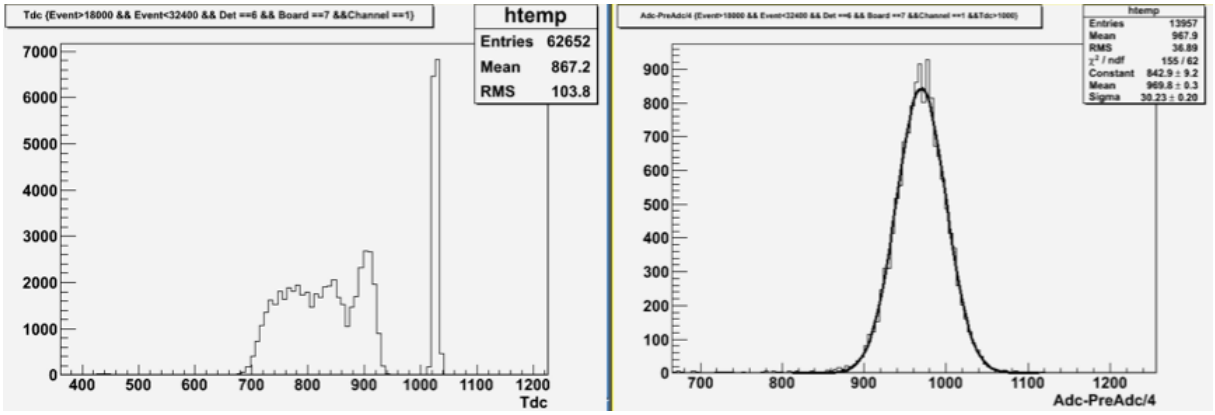


Figure 4.3: TDC and ADC of one PMT within one LED cycle.

by the gain calibration which has been calculated along with each run using real time data known as the rolling gain. Background readings of the PMT baseline, called the preADC, is subtracted from the ADC value and the number of p.e. is then calculated using the rolling gain. There are two types of ADC readout in the experiment, the coarse and fine grain ADC. The coarse grain applies to more energetic events for which the light produced is more intense, and the range in the fine grain ADC is not enough to record all the charge. The difference between coarse and fine grain ADCs is about 20 times. Calibration of the FEE

using a pulse generator, as well as, a fit to the data determined the rolling gain to be about 20 ADC/p.e. for fine grain and 400 ADC/p.e. for coarse grain[47].

To correctly select calibration data for the analysis, the following cuts are imposed,

- Number of received pulses from LED>14500 in only fine or coarse gain
- Trigger type is WPCalib
- TDC>$T_{min}$ and $\Delta$adc>300
- Only the earliest hit per PMT is taken

$T_{min}$ is the value of TDC in the trough after receiving the direct light, shown in fig.4.3. This value is different from tube to tube and is found by an algorithm which searches for the trough after the highest peak. $\Delta$adc refers to the ADC minus preADC value and 300 was determined by averaging many PMT $\Delta$adc readouts. It is high enough to cut out backgrounds due to accidentals while keeping the cut efficiency at almost 100%. The LED flashing frequency was set to be 300 Hz for 50 seconds and therefore each PMT in the direct line of sight should receive 15000 flashes. The condition of having more than 14500 flashes in either fine or coarse grain guarantees that PMTs are recording the charge in fine or coarse grain regime but not both as a mix of both coarse and fine grain would result in a non-linear $\Delta$adc readouts. Earliest hit to PMT means the highest peak of charge found by the PMT when a readout window of 1.2$\mu$s is opened after receiving the trigger.

Both local and global fits have been performed to the data selected. The local fit is a straight line to an LED event in various PMTs at various distances, according to equation 4.2 and figure 4.1. The slope in the fit represents the change between two runs while the y-intercept indicates the change in the LED initial intensity. In the WP, not all LEDs can cover PMTs at both long and short distances. Therefore only about one-forth of the LEDs were selected in the global fit to determine the relative changes in the attenuation length. The global fit incorporates all LED-PMT pairs used in the local fit and fits for the optimized slope but not the intercept. The $\chi^2$ function is defined as,

$$\chi^2 = \Sigma_{ij} \frac{(y_{ij} - (mx_{ij} + c_j))^2}{\sigma_y^2 + m^2\sigma_x^2} \tag{4.3}$$

where $j$ is the number of sets of local fit data and $i$ is the number of pairs used in each

set. The parameters m and $c_j$ are found by minimizing the $\chi^2$ function. The uncertainties $\sigma_x$ and $\sigma_y$ refer to the distance of LED-PMT pairs and $\Delta$adc respectively. The positions of LED are assigned a 5% uncertainty while the positions of the LEDs have a 1% uncertainty. The uncertainty of $\Delta$adc is simply taken from statistics, as $\sqrt{\Delta adc}$. The $\chi^2$ for two selected runs is shown in figure 4.4.

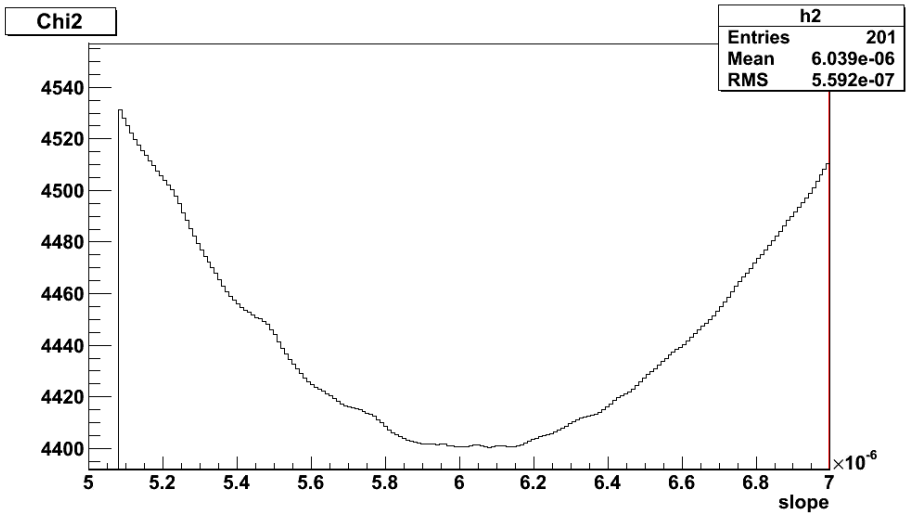


Figure 4.4: The $\chi^2$ fit of two runs. Minimum is at 6.08e-06. Wiggles around the minimum is due to the presence of $m^2$ in the denominator in the function.

The uncertainty of the slope is given by $\Delta\chi^2 = 1$ and the best fit slope is $6.08^{+0.08}_{-0.04} \times 10^{-6}$, which represents the difference of the inverse of the attenuation length measured in millimeter. If a particular run is chosen to be the base run and consecutive runs are calculated using this method, a time sequence of water clarity variation can be plotted for monitoring purpose. Figure 4.5 shows six weeks of consecutive runs relative to a baseline run. The IWS is not suitable for such monitoring due to the very strong reflection from AD and pipelines surfaces. Continuous monitoring in OWS has been halted because of the gradual failure of LED units. Absolute measurement using muon Cherenkov light has been proposed but effort has not been developed due to low PMT coverage from sparse distribution of PMTs in the

pool[48].

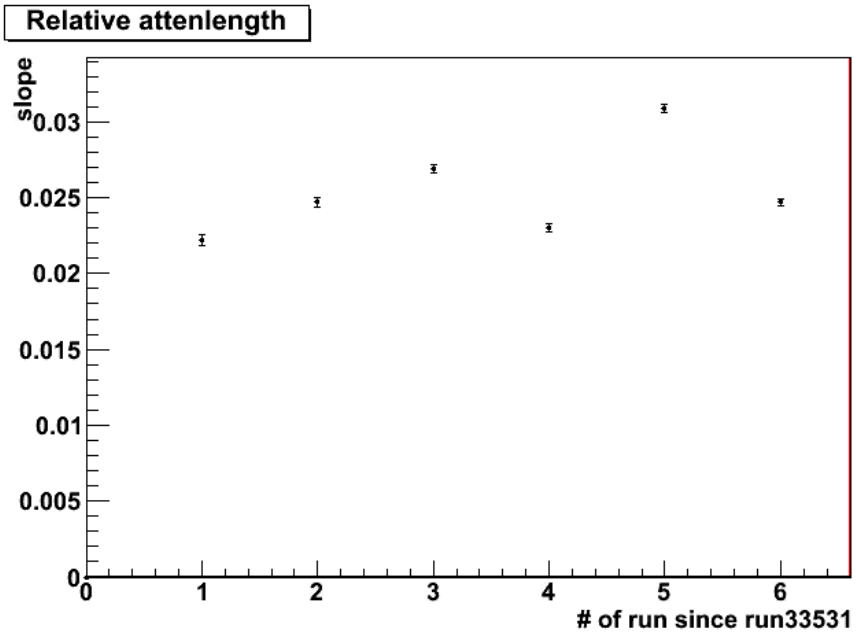


Figure 4.5: Changes in attenuation length in time sequence. Slope is in the unit of $m^{-1}$

# Chapter 5

# Spent Fuel Neutrino and Neutrino Spectrum Analysis

## 5.1 Nuclear Spent Fuel Neutrinos

Though the Daya Bay experiment is designed to measure electron anti-neutrinos emitted from isotopes in the reactor core under neutron irradiation, anti-neutrinos from other sources that exceed the detection threshold would also contribute to the overall statistics[49]. It is important to understand the impact from these neutrinos, especially at low energies, to the determination of $\sin^2 2\theta_{13}$. The principle of deficit detection is to compare the number of neutrinos collected at both the near and Far site and the ratio is related to the mixing angle based on equation 2.11. This ratio is,

$$\frac{N_f}{N_n} = \frac{N_{pf}}{N_{pn}}(\frac{L_f}{L_n})^2 \frac{\epsilon_f}{\epsilon_n} \frac{P_{ee}(L_f, E)}{P_{ee}(L_n, E)} \tag{5.1}$$

where $N_{f(n)}$ is the number of IBD events detected at the far(near) site, $N_{pf(n)}$ is the number of proton targets in the far(near) ADs, $L$ is the distance from the core to the AD, $\epsilon$ is the AD detection efficiency and $E$ is the neutrino energy.

The effect of spent fuel neutrinos(SFN) from each reactor core comes into play as an additional term to number of IBD events in each AD, at a given energy and time without oscillation,

$$N_{IBD}(E,t) = \frac{N_p(t)}{4\pi L^2}\epsilon(E,t)\sigma_{IBD}(E)\left(\Sigma_i\left(\frac{W_{th}(t)}{\Sigma_i f_i(t)e_i}f_i(t)S_i(E)c_{neq,i}(E,t)\right) + S_{SNF}(E,t)\right) \tag{5.2}$$

where $\sigma$ is the IBD reaction cross-section, $W$ is the thermal power, $f_i, e_i$ are the fission fraction and energy emitted from the i-th isotope, $S_i(E)$ is the number of neutrinos emitted by isotope $i$ at energy $E$, $c_{neq}$ is the non-equilibrium correction to $S_i(E)$ and $S_{SFN}(E,t)$ is the number of SFN emitted as a function of energy and time.

In normal reactor operation, one-third of the fuel rods are replenished after each fuel cycle, which is typically one year to 18 months at the Daya Bay complex. Cycled out fuel rods are stored in a giant water pool to further cool down for indefinite years. SFN, which are emitted with a decaying frequency, are detected by the ADs. The neutrino detection threshold of all ADs is 1.8 MeV, which corresponds to a 1.022 MeV in positron energy. A detection threshold of 0.7 MeV is accounted for finite resolution of IAV. There is an unknown amount of spent fuel rods in the storage water pool. The spectrum of SFN is predicted in figure 5.1.

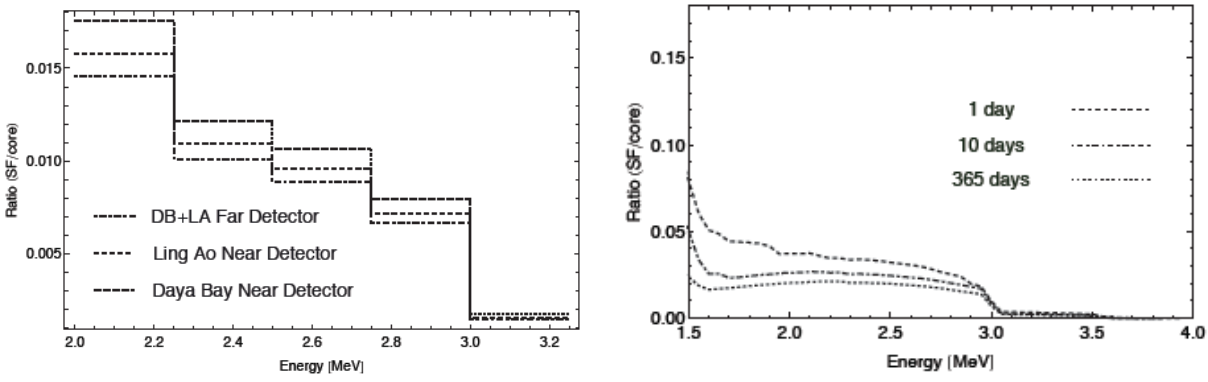


(a) SFN energy spectrum

(b) Non-equilibrium effect in SFN.

Figure 5.1: SFN energy spectrum and time dependence.[50]

Estimates on the contribution of SFN to the ADs are based on publicly available data from the IAEA. The SFN rate when the reactor is turned on ranges from 0.63% to 1.9% taking all spent fuel rods into account from the start-up of the cores[51]. In addition to rods in the spent fuel water pool, neutrinos from the rods in a core during a shutdown period are also contributing to the SFN in this analysis.

### 5.1.1 IBD Selection and Backgrounds

The data selection for this analysis is the same as for IBD events in the oscillation analysis[**?**]. The selection criteria are listed here:

• The flasher cut: reject spontaneous light emission from PMTs due to sudden base discharge[52].

• Energy: 0.7< $E_p$ <12.0 MeV, 6.0< $E_d$ <12.0 MeV

• Temporal separation: 1< $\Delta$t <200 $\mu$s

• Muon vetoes: $t_d - t_{\mu WS} < 600\mu s$, $t_d - t_{\mu AD} < 1ms$ or $t_d - t_{\mu sh} < 1s$

• Multiplicity: No additional >0.7 MeV trigger within $(t_p - 200\mu s, t_d + 200\mu s)$

$p, d$ and $\mu sh$ denote prompt event, delayed event and shower muon event. $\Delta$t is the time difference between prompt and delayed event which is the neutron capture time.

Figure 5.2a shows the prompt event spectrum after cuts and Fig. 5.2b shows the efficiencies of the cuts[53]. After selecting the prompt IBD event candidates, backgrounds must be subtracted from them. The major backgrounds are listed here:

• Accidental singles: Any pair of uncorrelated events that satisfy the IBD criteria. These singles are mainly from radioactivity inside the AD[54].

• Fast neutron: Originate from neutrons produced by cosmic ray muons passing near the AD[55]. An energetic neutron hits a proton causing it to recoil before the neutrino is captured, forming a prompt-delay pair.

• $^8He/^9Li$: These isotopes are products of muon spallation on carbon in AD[56]. The $\beta - n$ decays from these isotopes can fake an IBD event.

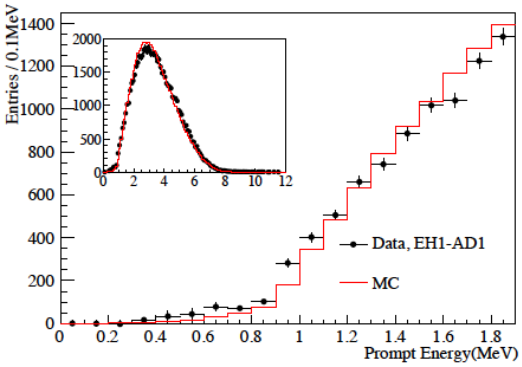


(a) IBD prompt energy spectrum in EH1 with accidentals subtraction, full range and enlarged.

| | Efficiency | Correlated | Uncorrelated |
|---|---|---|---|
| Target protons | | 0.47% | 0.03% |
| Flasher cut | 99.98% | 0.01% | 0.01% |
| Delayed energy cut | 90.9% | 0.6% | 0.12% |
| Prompt energy cut | 99.88% | 0.10% | 0.01% |
| Multiplicity cut | | 0.02% | <0.01% |
| Capture time cut | 98.6% | 0.12% | 0.01% |
| Gd capture fraction | 83.8% | 0.8% | <0.1% |
| Spill-in | 105.0% | 1.5% | 0.02% |
| Livetime | 100.0% | 0.002% | <0.01% |
| Combined | 78.8% | 1.9% | 0.2% |

(b) Efficiencies and uncertainties of each cut.

Figure 5.2: IBD prompt spectrum and cut efficiencies.[53]

• AmC in ACU: Neutrinos from the AmC source in the ACU on the top of AD make two types of backgrounds, alpha-n pair and two correlated gammas from inelastic scattering followed by capture on Fe.

• $^{13}C(\alpha, n)^{16}O$: Alphas from the decay chains of Th, K, U and Po, captured on $^{13}C$ and produce a neutron plus $^{16}O$[57].

The rates and spectra of the above backgrounds have been studied either with data or Monte Carlo. A summary of all rates is given in table 5.1.

Spectra of the five backgrounds and a combined plot are shown in figures 5.3 and 5.4.

| | EH1 | | EH2 | EH3 | | |
|---|---|---|---|---|---|---|
| | AD1 | AD2 | AD3 | AD4 | AD5 | AD6 |
| IBD candidates | 101290 | 102519 | 92912 | 13964 | 13894 | 13731 |
| DAQ live time (days) | 191.001 | | 189.645 | 189.779 | | |
| $\epsilon_\mu \cdot \epsilon_m$ | 0.7957 | 0.7927 | 0.8282 | 0.9577 | 0.9568 | 0.9566 |
| Accidentals (per day) | 9.54±0.03 | 9.36±0.03 | 7.44±0.02 | 2.96 ± 0.01 | 2.92 ± 0.01 | 2.87 ± 0.01 |
| Fast-neutron (per AD per day) | 0.92±0.46 | | 0.62±0.31 | 0.04±0.02 | | |
| $^{9}$Li/$^{8}$He (per AD per day) | 2.40±0.86 | | 1.20±0.63 | 0.22±0.06 | | |
| Am-C correlated (per AD per day) | 0.26±0.12 | | | | | |
| $^{13}$C(α, n)$^{16}$O background (per day) | 0.08±0.04 | 0.07±0.04 | 0.05±0.03 | 0.04±0.02 | 0.04±0.02 | 0.04±0.02 |
| IBD rate (per day) | 653.30±2.31 | 664.15±2.33 | 581.97±2.07 | 73.31 ± 0.66 | 73.03 ± 0.66 | 72.20 ± 0.66 |

Table 5.1: Rates of backgrounds and IBD in all ADs [53]

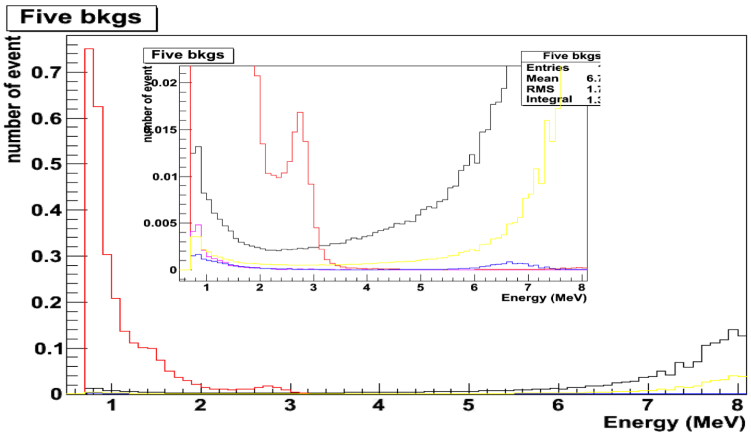


Figure 5.3: Spectra of the five major backgrounds.

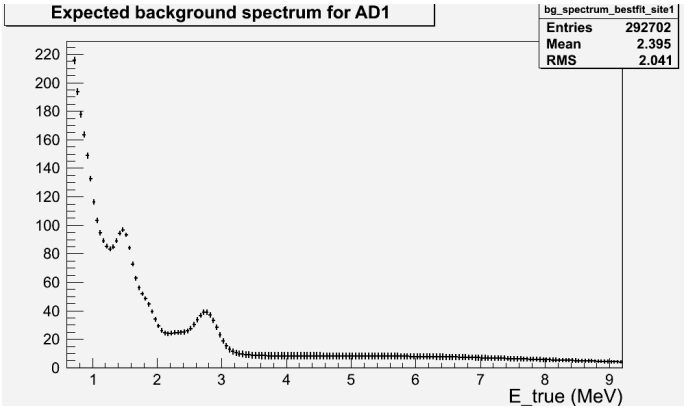


Figure 5.4: A fit of the combined background, dominated by singles.

### 5.1.2 SFN Analysis

In this analysis, only the EH1 ADs are used for which the DYB cores contributed about 78% of all detected neutrinos. Since SFN only accounts for a very small amount of the events detected in an AD, we assumed that the entire SFN contribution is from the DYB cores only. This assumption works because of the inverse square distance effect and the power history of LA cores are relatively short. SFN from the DYB cores include the sum of SFN

from the spent fuel storage pool and all neutrinos from the fuel rods in a shutdown core. A two-bin analysis is performed to track for the contribution of SFN at low energy with an upper energy bound is set at 2.4 MeV, in positron energy. The bin below 2.4 MeV contains SFN while the the bin above does not.

The idea is to look for a small difference in the two bins by taking a ratio of two data sets. The first data set includes all periods when one of the two DYB cores was shutdown while the second data set includes periods where all six cores were in operation. The higher energy bin of the two sets should be in proportion to the live time of that data set and the lower energy bin should have a relatively larger ratio due to the SFN contribution. There are two major issues in this analysis. The two data sets come from different stages in fuel cycles of all six reactor cores and the core produces more low energy neutrinos as it burns which may affect the ratio. The second issue is the effect of oscillation on the two bins. Although the four LA cores provide only 22% of all detected neutrinos in the two ADs, those neutrinos arrive at the ADs closer to their oscillation maximum and could contribute differently to the two energy bins.

A MC simulation was built based on the predicted flux[58] to study the effect of oscillation from different cores to the EH1 ADs. This MC package incorporates all factors listed in equation 5.2, except for the non-equilibrium effect, using cross-section extrapolation and flux models available[59]. The correction for oscillations is done by first getting the effective oscillation curve using the MC with the same live-time as in the data sets and then applying this curve to the data sets. The effective oscillation of six ADs is defined to be the ratio of the event rates as a function of energy with the oscillation probability to the one without.

$$P(E) = \frac{\Sigma_{i=1}^{6} N_i(E, L_i) P_{ee,i}(E, L_i)}{\Sigma_{i=1}^{6} N_i(E, L_i)} \tag{5.3}$$

Figure 5.5 shows the effective oscillation curve determined from the MC samples. In the MC, the value used for $\sin^2 2\theta_{13}$ comes from our first rate-only analysis results[53].

To understand the effect of oscillations on the SFN, the oscillation is turned on and off in the two selected MC samples equivalent to the data sets with the manual addition of SFN

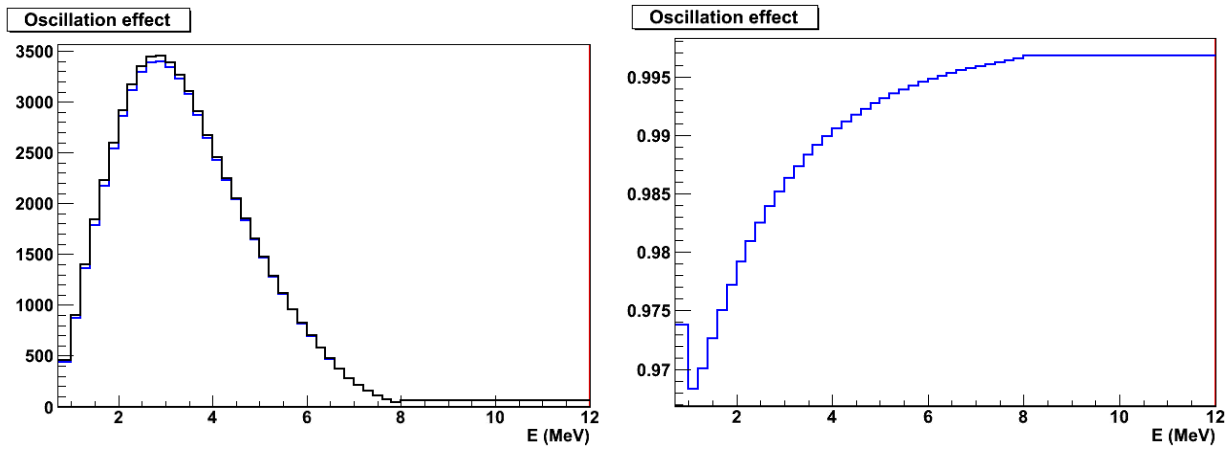


Figure 5.5: Effective oscillation using MC samples. The left is the IBD prompt spectra with(out) oscillations. The right is the effective oscillation curve with the first bin below 1 MeV.

to the DYB core shutdown period. The amount of SFN added is arbitrary but sufficient to make the ratio of first bin higher than the second. The effect of oscillations in the MC results is to shrink the deviation between the two bins, as shown in figure 5.6.

The plot indicates that the presence of oscillations hides the contribution of SFN by suppressing the lower energy bin. The red line in the plot has the first bin 0.38% higher than the second while the blue line is only 0.07% higher. The difference in red-blue is 0.69% in the first bin and 0.38% in the second. This suppression is a result of a larger oscillation amplitude at lower energy as shown in the effective oscillation curve, shown in fig.5.5b.
The second effect on SFN detection is that each reactor has its own fuel cycle. DYB cores have an 18 month cycle while LA core cycle is 12 months. When a core is refueled, it is shutdown for about five weeks. Only one core of each pair is refueled at a time. This fuel cycle poses a problem in that the 2-bin analysis of neutrinos detected in ADs in EH1, including SFN, could be interrupted if any core in those data sets were refueled. A new fuel batch produces more high energy neutrinos than an older fuel batch and this difference disturbs the 2-bin comparison regardless of oscillations.

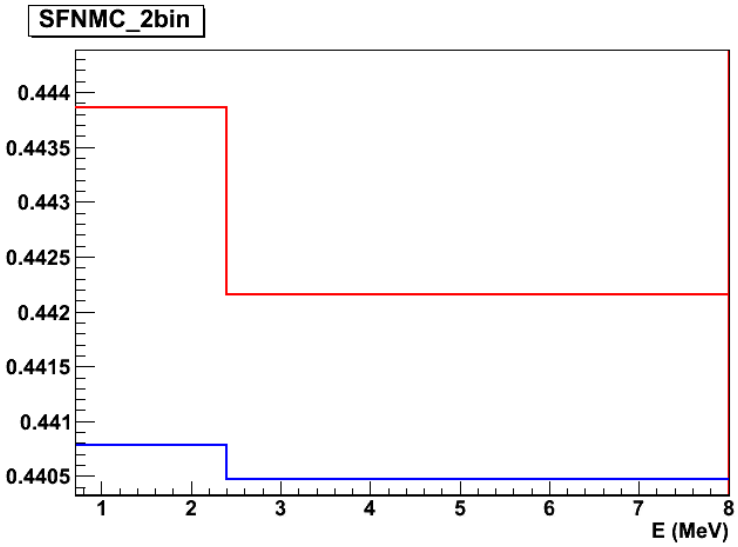


Figure 5.6: Simulation of oscillation effect on SFN in EH1. The red line is without oscillations and the blue line includes oscillations. The horizontal axis is in positron energy.

Figure 5.7 showed how the ratio of neutrinos from single core (D1) in near site changes as a function of energy with respect to both DYB cores. This MC simulation uses the flux prediction consistent with the measurement and the plot shows a drop in production at high energy.

With reference to D1 above, with different cores at different stages in the fuel cycle results in different contributions to the overall spectrum in the 2-bin analysis and therefore compromises the assumption that all core were operating in the same way during the data set selected. Figure 5.7b shows the 2-bin analysis without adding SFN from the shutdown core, the effect of the oscillation and fuel cycle resulted in the second bin being higher than the first.

Applying the 2-bin analysis to the data with 76 days of 5 cores and 103 days of 6 cores, the plot, shown in fig. 5.8 was not oscillation corrected, as the stage in different fuel cycles are not known. The uncertainties of both bins are propagated from the statistics of IBD and the five backgrounds. Figure 5.8 has the first bin higher than the second by 0.7% which is

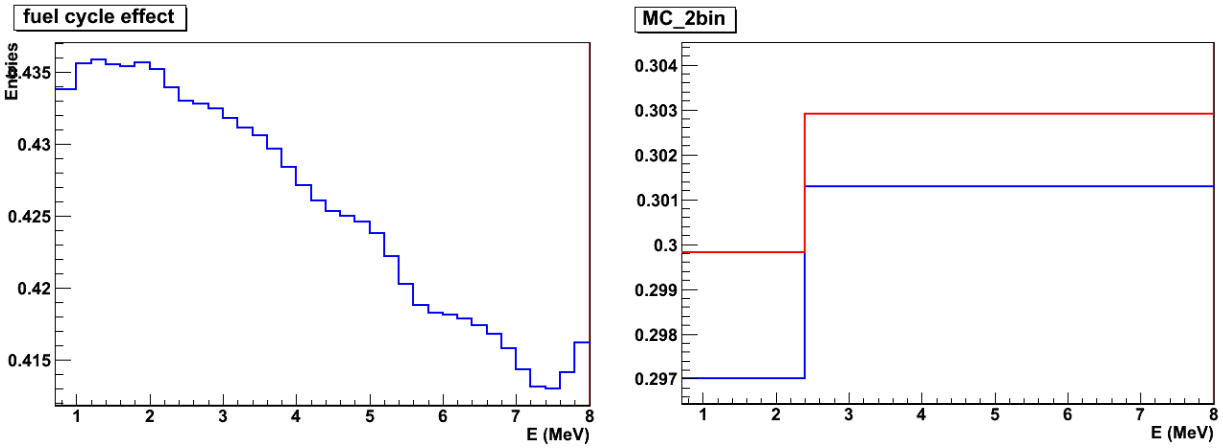


Figure 5.7: Fuel cycle effect from MC simulation. The left is the ratio of one core to two cores of DYB reactor based on flux prediction. The right is the MC with one DYB core shutdown. Red(Blue) denotes oscillation off(on)

less than the combined uncertainty of 1.3% from both bins. Since the uncertainty is larger than the measured difference, it is insufficient to make a measurement of SFN. Applying the oscillation correction alone without correcting for fuel cycle effect cannot accurately describe the scenerio. More data are needed to increase the statistics and suppress the uncertainty.

## 5.2 Generic Reactor Neutrino Spectrum

The Daya Bay experiment was successful in measuring the last unknown neutrino mixing angle, $\theta_{13}$, by employing a two detector setup. In addition to that, the high thermal power of all reactor cores enables a precise measurement of the electron antineutrino spectrum. This spectrum could be useful for future reactor experiments to make a prediction of their flux based on the thermal power of the reactor complex and the fission isotope composition. Therefore, this analysis aims to provide a background subtracted, non-linearity and oscillation corrected and normalized spectrum using multiple ADs with an energy binning of 0.25 MeV. Moreover, the effective fission fraction, with respect to the data period of the

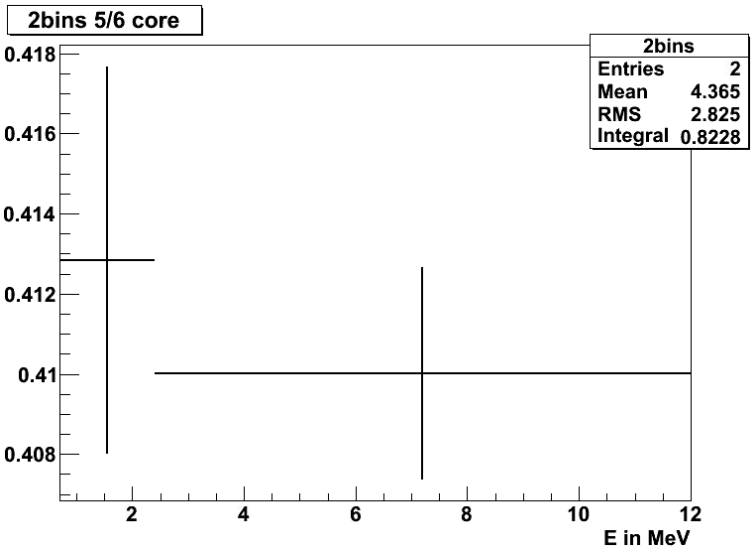


Figure 5.8: The 2-bin analysis of data. The data period of the 5 core running is 76 days combining shutdown time of either DYB cores and the 6 cores is 103 days.

spectrum, is calculated using the information supplied by the power company to make the spectrum scalable for other experiments to use.

### 5.2.1 Electron Anti-neutrino Spectrum

As shown in the SFN analysis, there are long-lived and short-lived beta-decay isotopes in the fuel rod. These isotopes could be traced back to four main components: $^{235}U$,$^{238}U$,$^{239}Pu$ and $^{241}Pu$. The composition of four isotopes is given as four fission fractions which are provided by the power company on weekly basis. To convert the measured positron spectrum to a neutrino spectrum, the following steps were developed.

- Extract the positron spectrum from the IBD selection,
- Subtract backgrounds,
- Make a non-linearity (NL) correction,
- Convert from positron energy to neutrino energy,
- Correct for oscillation of the neutrino spectrum, and

• Combine spectra from the three ADs.

For the first three steps, one can either do the NL correction before or after subtracting the backgrounds, event-by-event at tree level in the code. In this analysis, this correction is performed after the subtraction using a matrix with a bin size of 0.05 MeV. The NL model used for the official analysis is the IHEP one[41] and is shown in figure 5.9a. The origins of non-linearity in the AD are: 1) IBD events that occur inside the material of IAV and disrupt the production of scintillation light and 2) the minimum energy deposition of high energy positrons traversing the IAV and 3) the non-linearity from electronics. The effect of applying the NL correction is an energy re-distribution, shown in figure 5.9b.

The conversion from positron energy to neutrino energy is performed by mapping the positron spectrum onto the neutrino spectrum with a 240-by-240 matrix. This matrix employs gaussian smearing of every energy bins and is normalized with respect to the highest bin. Therefore, it represents the probability of having a certain number of events in neutrino energy bin given events in a particular positron energy bin. Theoretical speaking, this energy conversion should be diagonal based on the kinematics of inverse beta decay, (equation 2.12). However the convolution of the IAV NL effect contributes off-diagonal elements in this matrix. The NL correction is incorporated into this energy conversion matrix which is shown in figure 5.10.

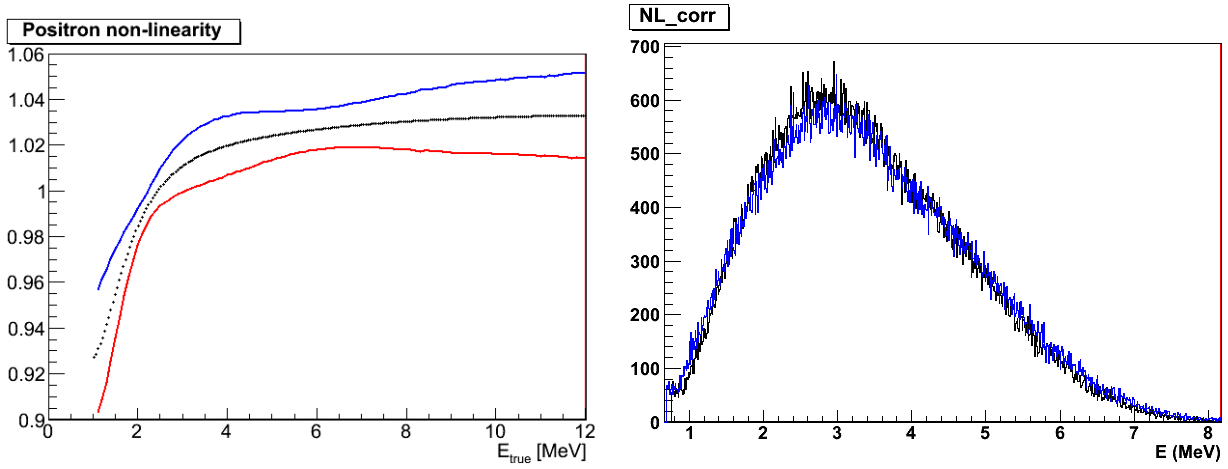


(a) Nominal NL model. Blue(Red) are upper(lower) limits of the model.[41]

(b) NL correction narrows the energy spectrum of the positron. Black(Blue) denotes after(before) correction.

Figure 5.9: Non-linearity model and correction to positron spectrum.

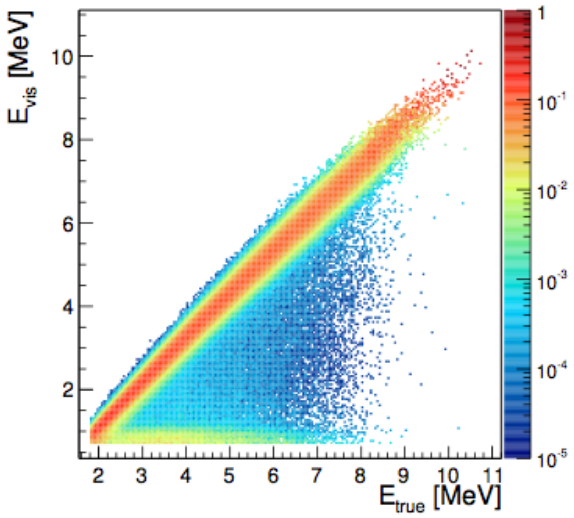


Figure 5.10: Conversion matrix from positron energy to neutrino energy[60].

Using this matrix[60], each energy bin in the positron spectrum is multiplied by the corresponding row of the matrix and then summed over each neutrino energy column to gen-

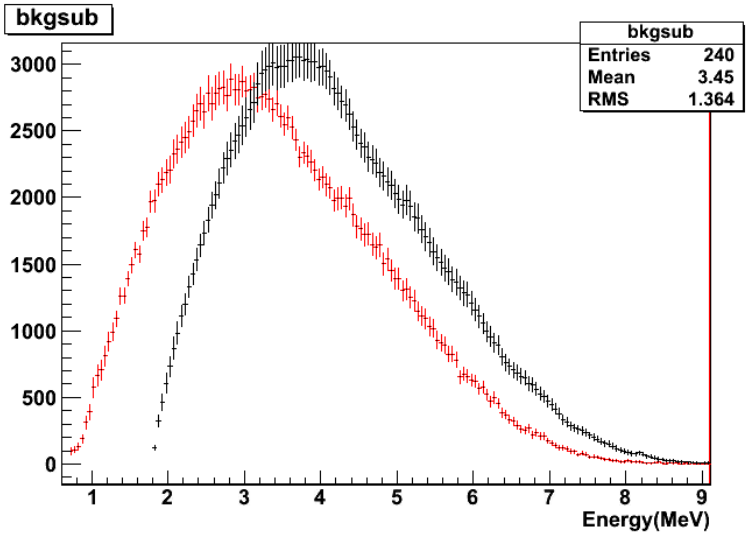


Figure 5.11: Energy conversion of positron(neutrino) spectrum. Red(Black) is before(after) conversion in positron(neutrino) energy.

erate the neutrino spectrum. The positron spectrum, starting from 0.7 MeV, is converted to neutrino energy starting from 1.8 MeV. Figure 5.11 shows the spectra before and after conversion. Since all ADs are functionally identical, the conversion and NL correction are applied to all ADs at all experimental sites without further weighting.

The converted electron anti-neutrino spectrum represents the neutrino spectrum measured at AD from the cores. An oscillation correction is needed for each AD since the baselines are different. The correction is based on the one described in the SFN section. This correction is similar to figure 5.5 since the method and flux prediction used in MC are the same but the spectrum for this analysis is in neutrino energy instead of positron energy.

To get a high statistics spectrum, the results from each AD are added up with weights from their target mass, thermal power and detection efficiency. Only six ADs were in operation for the data set analyzed, two in EH1, one in EH2 and 3 in EH3. The 3 ADs in EH3 combined contributes about 10% of all events and therefore are not used in this analysis. Table 5.1 shows the IBD rate and detection efficiencies of all six ADs in the data set. The number of target protons is basically equivalent of saying the number of hydrogen within the IAV

and is measured to be $1.43 \times 10^{30}$ with an uncertainty of 0.47%. The thermal power of each core is provided by the power company together with fission fractions. The weighting factor applied to thermal power is the live-time of the three ADs in weeks extrapolated from days to match the weekly-released thermal power. The distance effect of each AD has been taken into account in the effective oscillation correction in neutrino energy.

The final combined neutrino spectrum is given in figure 5.12. This spectrum shows the three ADs combined, background subtracted, NL and oscillation corrected and normalized, in the units of $\bar{\nu}_e cm^2/proton/MeV/fission$.

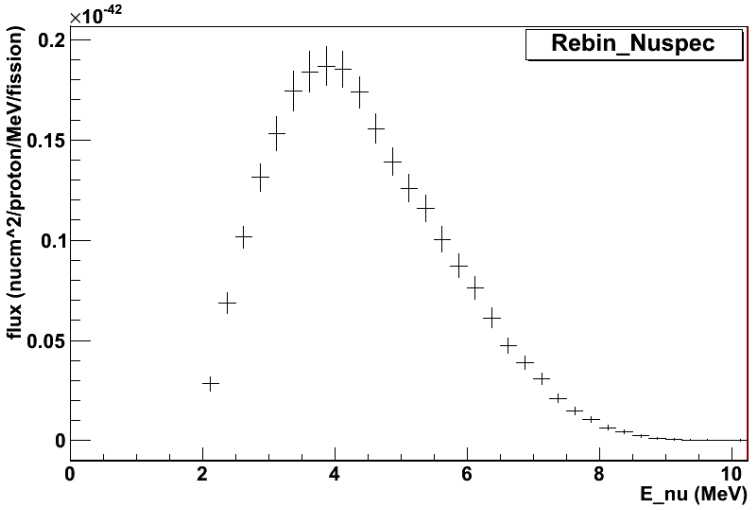


Figure 5.12: The normalized electron anti-neutrino spectrum, binned in 0.25MeV.

### 5.2.2 Effective Fission Fraction

The effective fission fraction refers to the weighted fission fraction of the all cores in the 3-AD spectrum across the data period. This effective numbers served as a reference for other experiments to make prediction of what their reactor spectrum should look like by scaling their fission fractions with respect to the Daya Bay measurement. Since each reactor experiment would have different baselines and thermal powers, the effective fission fractions

calculated here have units of length and power.

The Daya Bay reactors have a nominal thermal power of 2895 MW and the power company reports the weekly power as a percentage of the nominal power. The weekly fission fractions of the four isotopes are also reported as percentages. Fresh fuel rods typically have highest content of $^{235}U$, approximately 72%, which gradually burns up throughout the cycle. $^{239}Pu$ and $^{241}Pu$ gradually increase in fractions while $^{238}U$ mostly remains unchanged. The fission fraction is a measure of the isotope, in percentage, which is fissionable in a fuel cycle. The energy released in each fission is proportional to the electricity generated and is tabulated below[59].

The definition of effective fission fraction, $F_i$ of the i-th isotope, is as follow,

| | $^{235}U$ | $^{238}U$ | $^{239}Pu$ | $^{241}Pu$ |
|---|---|---|---|---|
| fresh fuel % | 73.9 | 7.4 | 16.0 | 2.7 |
| used fuel % | 45.4 | 7.7 | 38.2 | 8.7 |
| energy released (MeV) | 201.9 | 205.52 | 209.99 | 213.60 |

Table 5.2: Fission fraction by isotope and the energy released per fission.[59]

$$F_i = \frac{f_i}{S_f} \tag{5.4}$$

$$f_i = \Sigma_{AD=1}^{3}\Sigma_{r=1}^{6}\left(\frac{W_r}{4\pi L_{rAD}^2}\frac{f_{ir}}{\Sigma_{k=1}^{4} f_{kr}e_k}\right) \tag{5.5}$$

$$S_f = \Sigma_{i=1}^{4} f_i \tag{5.6}$$

where the indexes AD and $r$ refer to ADs and reactor cores, $f_{ir}$ is the provided fission fraction of the i-th isotope in the r-th core, $e_k$ is the energy released per fission for isotope $k$, $W_r$ is the thermal power of the r-th reactor core, $S_f$ is the sum of the calculated fission fractions and $L$ is the distance from core to AD.

In addition to the above parameters, the sum is performed with a cumulative week of released data over the period of data used and weighted with the detector live-time calculated

separately. Figure 5.13, shows the time series of fission fractions in each core. Discontinuities in the dotted lines are from times when the cores are restarted after refueling. The solid black lines are the thermal power.

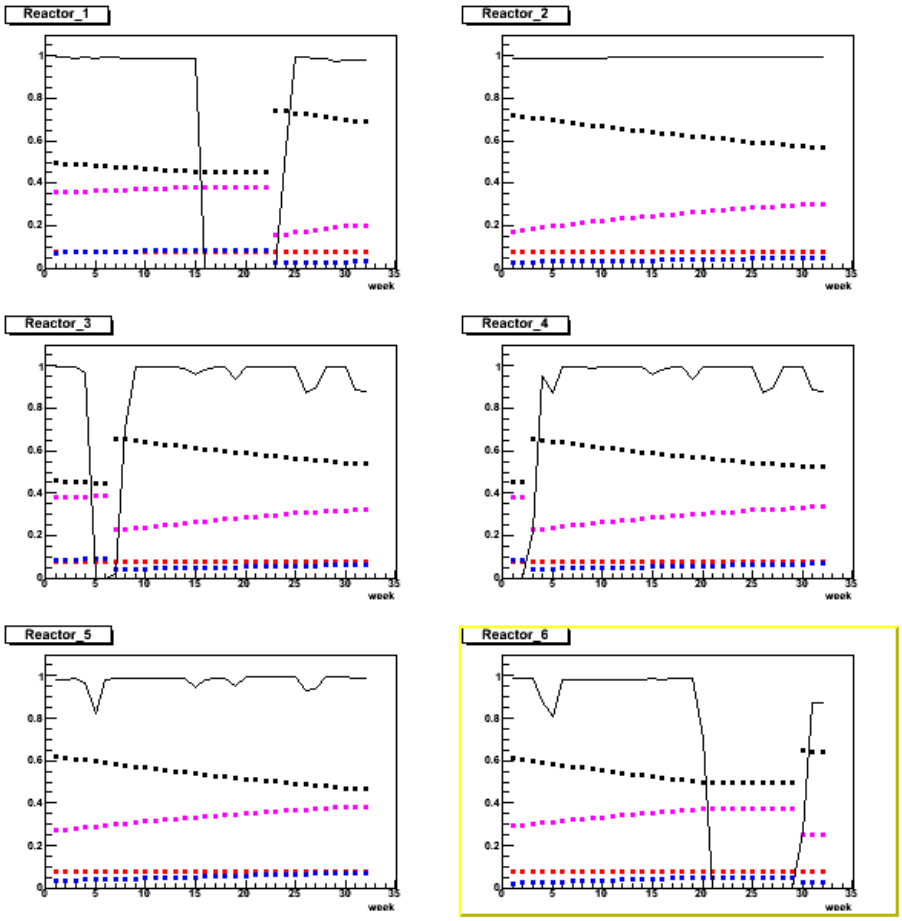


Figure 5.13: Fission fraction for each core over the data period. The black, red, purple and blue are respectively U235, U238, Pu241 and Pu239. The solid black lines are fractional thermal power.

Figure 5.14 is the time dependent effective fission fraction calculated over the data period. Since the plotted points are an accumulation of weekly numbers, the fuel cycle effects are washed out and converging. The uncertainties on the plot points are calculated based on

equations 5.4-5.6. Each parameter in the formulae has its own uncertainties listed below. Uncertainties on the baselines are being ignored in the calculation. The uncertainties in the plot are the diagonal values of the covariance matrix calculated from the formulae. The four isotopes converge to stable values even with the refueling. This long term behavior defines the burn-up profile of the reactors within the data period.

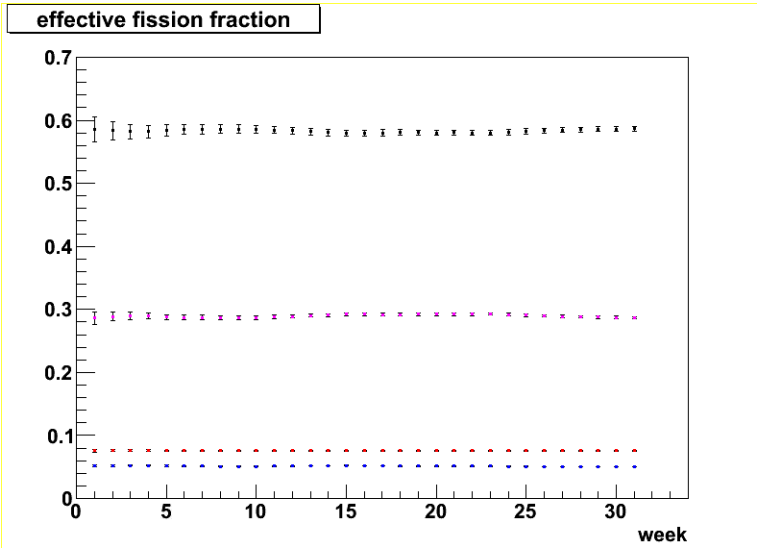


Figure 5.14: Effective fission fractions of the 6-core as measured by the 3-AD given as a function of time.

| | $W_r$ | $f$ | $e$ | $L$ |
|---|---|---|---|---|
| uncertainty % | 0.6 | 5 | 0.2 | 0.01 |
| | $^{235}U$ | $^{238}U$ | $^{239}Pu$ | $^{241}Pu$ |
| $F_i$ % | 58.55 | 7.60 | 28.81 | 5.04 |

Table 5.3: Uncertainties on reactor parameter and values of the cumulative effective fission fractions.

### 5.2.3 Uncertainty Analysis

The uncertainties of the generic spectrum and the associated cumulative fission fractions are detailed here. For the generic spectrum, the final uncertainty is a convolution of:

- The IBD statistical and systematical uncertainties
- Backgrounds statistical and systematical uncertainties
- Non-linearity model systematical uncertainties
- Energy conversion statistical uncertainties
- Effective oscillation systematical uncertainties

The first two items are understood from the rate+shape analysis of the $\sin^2 2\theta_{13}$[38].

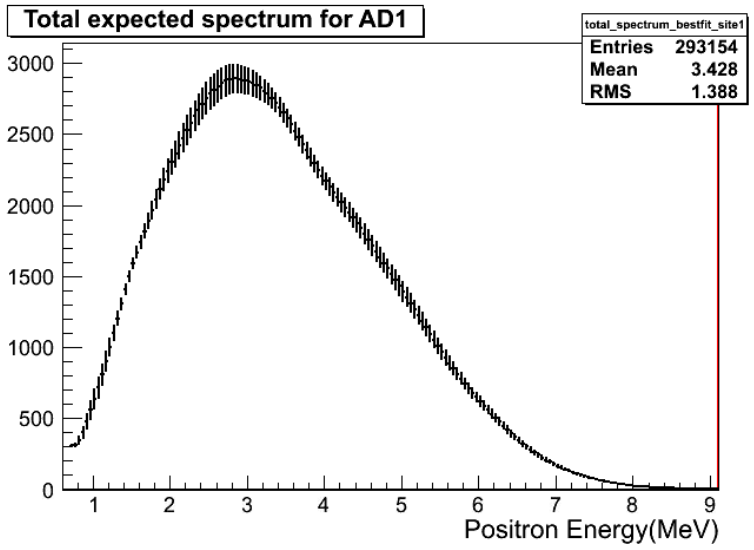


Figure 5.15: IBD spectrum with systematics and all uncertainties.

The impact from the last three items to the generic spectrum is previously known. To study these effects when converting the positron spectrum to neutrino spectrum, a MC was constructed. Two sets of inputs are implemented into the MC: the first is a fluctuation of the positron spectrum to estimate the effect on the neutrino spectrum, as shown in figure 5.16, and the second is a fluctuation of the NL model embedded in the energy conversion matrix

according to the upper and lower bounds of the curve, in figure 5.9a. The Root-Mean-Square value of each bin in the neutrino spectrum is calculated given variations of the two inputs in each bin. The results are shown in table 5.4,

| | Matrix elements | $e^+$spec |
|---|---|---|
| variation on bins | $\pm 4\%$ | $\pm$1-sigma |
| RMS on Nu-spec | $< 1\%$ | 3% |

Table 5.4: RMS on each bin of neutrino spectrum due to variations on inputs.

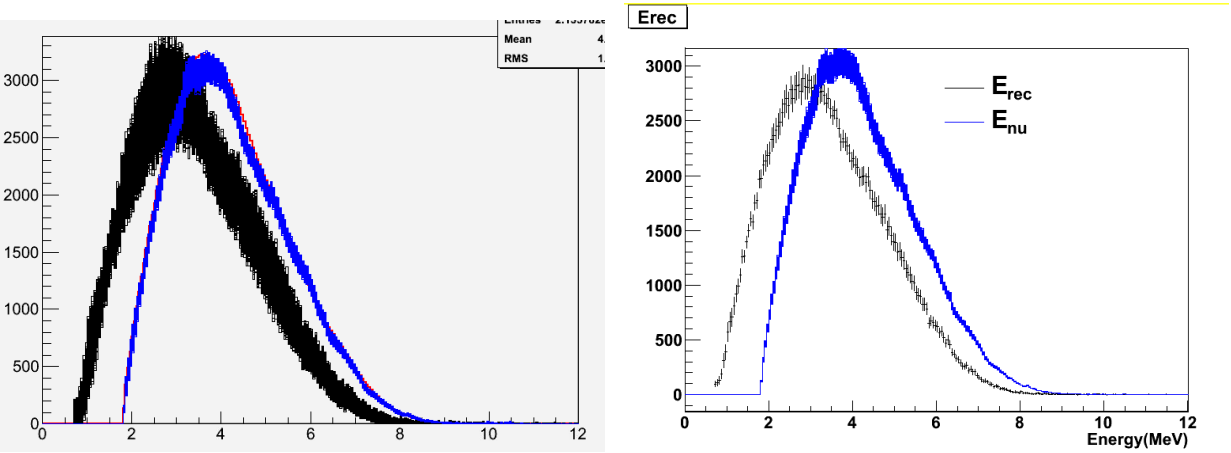


Figure 5.16: Effect on neutrino spectrum using MC variation on positron spectrum and NL model. The left is the variation on the positron spectrum. The right is the variation on the non-linearity model

The above two simulations only estimate the uncertainties introduced to neutrino spectrum due to these two effects. The conversion from positron to neutrino involves the unfolding process for which the bias is not accurately known and is being studied[61]. Uncertainty from oscillations is based on equation 2.11 and is formulated as,

$$\sigma_{osc} = \frac{1 - P_{ee}}{P_{ee}} \frac{\sigma_{sin^2 2\theta_{13}}}{sin^2 2\theta_{13}} \tag{5.7}$$

The value of $\sin^2 2\theta_{13}$ and the associated uncertainty are the measurement made by Daya Bay and thus the uncertainty from oscillation is about 0.6% depending on the AD.

The overall uncertainties, from IBD selections to oscillation correction, and the adding up three ADs, including the unfolding process, is given by a covariance matrix[61]. The MC shown in figure 5.16 is complementary to the uncertainty propagation in showing how much changes on the positron spectrum and NL model affect the unfolding. The covariance matrix of the cumulative fission fractions is also calculated using a covariance matrix of fission fractions and the Jacobian relating other variables. The final results is shown in figure 5.17 and table 5.5.

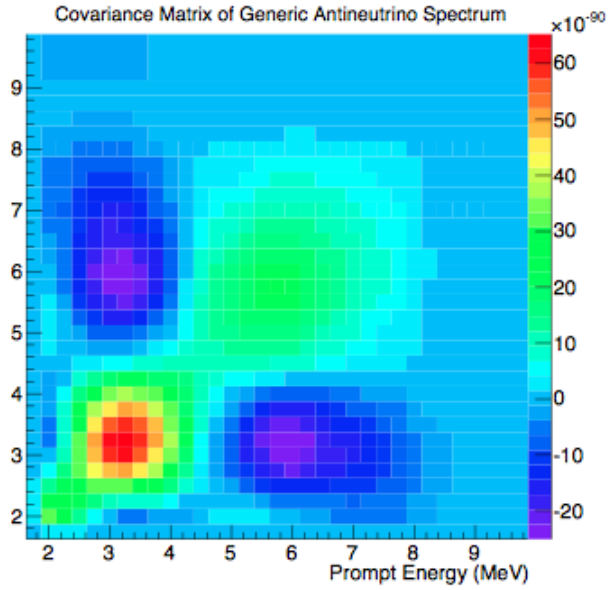


Figure 5.17: Covariance matrix of neutrino spectrum over 3-AD[62].

| | $^{235}U$ | $^{238}U$ | $^{239}Pu$ | $^{241}Pu$ |
|---|---|---|---|---|
| $^{235}U$ | 8.482e-05 | -2.401e-06 | -1.940e-05 | -8.350e-07 |
| $^{238}U$ | -2.401e-06 | 1.434e-06 | 9.040e-07 | 2.302e-07 |
| $^{239}Pu$ | -1.940e-05 | 9.040e-07 | 1.871e-05 | 1.540e-06 |
| $^{241}Pu$ | -8.350e-07 | 2.302e-07 | 1.540e-06 | 6.082e-07 |

Table 5.5: Covariance matrix between fission fractions[62].

# Chapter 6

# Summary of the Daya Bay Experiment

## 6.1 The Daya Bay Results and Beyond

The Daya Bay reactor electron anti-neutrino experiment has successfully measured $\sin^2 2\theta_{13}$, the last unknown mixing angle in PMNS matrix. It provides the most precise determination on the value, in addition to the shape of anti-neutrino spectrum (shown in figure 6.1). From equation 5.1, the Near-Far detector measurement gives a clear deficit at the far site due to neutrino oscillation. We find:

$$R = 0.944 \pm 0.007(stat) \pm 0.003(sys)[53] \quad (6.1)$$

$$\sin^2 2\theta_{13} = 0.090^{+0.008}_{-0.009}[63] \quad (6.2)$$

$$|\Delta m^2_{ee}| = 2.59^{+0.19}_{-0.20} \times 10^{-3} eV^2[63] \quad (6.3)$$

$$\sin^2(\Delta m^2_{ee}\frac{L}{4E}) = \cos^2\theta_{12}\sin^2(\Delta m^2_{31}\frac{L}{4E}) + \sin^2\theta_{12}\sin^2(\Delta m^2_{32}\frac{L}{4E}) \quad (6.4)$$

Another similar experiment, RENO[14], in South Korea, has also published similar results to Daya Bay which serves as an independent validation of reactor neutrino measurement.

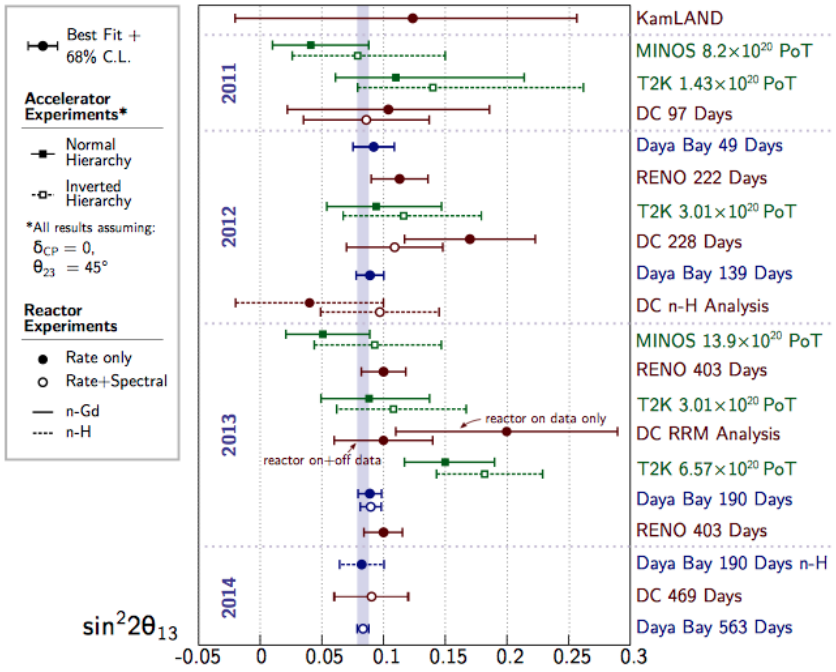


Figure 6.1: Comparison of measurements of $\sin^2 2\theta_{13}$ by various experiments showing that Daya Bay has the world-leading precision.[42].

A precise measurement of the mixing angle and spectrum is not only beneficial to the completion of standard model, but also provides a solid test for various theories and models of neutrino spectra from radioactive isotopes in reactor core. Several models have been proposed based on theories and past experiments to predict the neutrino flux from the four major isotope as described in chapter 5[59]. The generic neutrino spectrum is the ideal way to test those predictions[64]. A further analysis, extending from the generic spectrum described in the last chapter, is a possible decomposition of the measured spectrum into isotope spectra using the given fission fractions[65]. A fitter has been setup but it was very sensitive to small changes in the fission fraction of U-238, which makes the decomposition matrix singular. A method of singular value decomposition(SVD) is proposed to tackle this issue. Since the data taking of Daya Bay started from December 2011 and the fuel cycle of cores are typically 18 and 12 months, there have only 2 to 3 fuel cycles elapsed. This makes

the decomposition very tricky to resolve.

In addition to reactor related physics, the experiment is able to give bound on the existence of sterile neutrinos[66]. Another $\sin^2 2\theta_{13}$ analysis based on nH capture which has very different treatment on the backgrounds and IBD selections has been completed[67]. The full 8-AD configuration is also being used as a supernovae activity warning system to forecast potential supernova explosion based on earlier arrival of neutrinos[68] relative to photons.

The large value of $\sin^2 2\theta_{13}$ measured in Daya Bay significantly brightens the prospect for the future accelerator neutrino experiments. In the shorter term, T2K[69] and NO$\nu$A[70] may have the ability to detect the neutrino mass hierarchy and possibly determine the CP phase, $\delta_{CP}$. Otherwise, the next generation of long-baseline experiments, such as LBNE[71], LENA[72] and HyperK[73], are designed to measure these parameter over most possible parameter space. The impact of a large $\theta_{13}$ is also felt widely in theoretical neutrino physics. With $\sin^2 2\theta_{13} = 0.097$, the number of neutrino mass and mixing models in agreement with experimental results is greatly reduced from 40 to around 7[74]. In addition, previously favored tri-bimaximal mixing schemes, which require an almost-null value of $\theta_{13}$, are rejected. The significant constraints on CP-violation and the mass hierarchy expected from future experiments because of a large $\theta_{13}$ will further reduce this number. Other reactor experiments, such as JUNO[75] and RENO-50[76], are under consideration in China and S.Korea to measure the mass hierarchy with an intermediate baseline. This work was triggered by the success of the Daya Bay experiment.

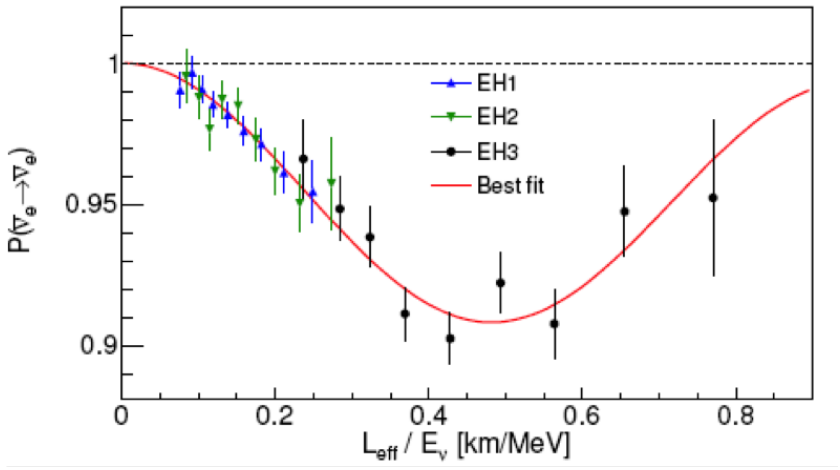


Figure 6.2: Measured neutrino oscillation in Daya Bay.[63].

## 6.2 Thesis Summary

This thesis covers the historical development of neutrino physics, starting from the proposal of a new hypothetical particle to preserve energy conservation in beta decay to the solar neutrino problem that eventually led to a confirmation of neutrino oscillations and therefore flavor interference phenomenon. Several previous reactor experiments of particular importance were briefly described with their best measurements on oscillation and neutrino flux. The urge for a precise measurement of $\theta_{13}$ has pushed experiments like Daya Bay, RENO and Double Chooz to adopt a near-far relative measurement at short baseline to a high thermal power reactor complex using metal-loaded liquid scintillator, with heavy rock overburden. The layout and detector design of the Daya Bay experiment has been detailed together with calibration methods and detector response.

Analysis of the data collected is not limited to the search for oscillations (mixing angle and corresponding mass square difference), but also to other physics such as cosmic muon flux, muon spallation production and detector related physics such as PMT calibration, optical attenuation in water and RPC R&D. Our particular physics interest is on the reactor neu-

trino spectrum, spent fuel neutrino contribution and a potential to decompose the generic spectrum into isotope spectra for future reactor safeguard purpose. Further developments on nH analysis, sterile neutrino detection bound and early supernova warning are ongoing. The measurement of Daya Bay experiment has superseded all past ones in precision. The results on the mixing angle, spectrum and reactor related information provides future experiments with not only a better plan for neutrino physics experiments due to large angle but also a high quality flux prediction based on our results. Further accumulation of data in the next two years will maintain our world-leading precision and provide tighter constraints on the parameter $|\Delta m^2_{32}|$ which will be beneficial to accelerator experiments. Issues such as the reactor anomaly, CP-violating phase and mass hierarchy will be resolved on the basis of the Daya Bay measurement in this high precision era.

# Bibliography


[1] Benjamin W. Lee Ernest s. Abers. Gauge theories. *Physics Reports*, 9:1–2, Sep 1973.

[2] David Griffiths. *Introduction to Elementary Particles*. WILEY_VCH, 2 edition, 2008.

[3] F. A. Scott. Energy spectrum of the beta-rays of radium e. *Phys. Rev.*, 48:391–395, Sep 1935.

[4] B. Pontecorvo. Inverse beta-decay process, 1946.

[5] U. Dore and L. Zanello. Bruno Pontecorvo and neutrino physics. `http://arxiv.org/abs/0910.1657`.

[6] C.L. Cowan, F. Reines, F.B. Harrison, H.W. Kruse, and A.D. McGuire. Detection of the free neutrino: A Confirmation. *Science*, 124:103–104, 1956.

[7] Raymond Davis, Don S. Harmer, and Kenneth C. Hoffman. Search for neutrinos from the sun. *Phys. Rev. Lett.*, 20:1205–1209, May 1968.

[8] John N. Bahcall. Solar models: An Historical overview. *AAPPS Bull.*, 12N4:12–19, 2002.

[9] B. Pontecorvo. Neutrino Experiments and the Problem of Conservation of Leptonic Charge. *Sov.Phys.JETP*, 26:984–988, 1968.

[10] Super-Kamiokande Collaboration. Evidence for oscillation of atmospheric neutrinos. *Phys. Rev. Lett.*, 81:1562–1567, Aug 1998.

[11] SNO Collaboration. Direct evidence for neutrino flavor transformation from neutral-current interactions in the sudbury neutrino observatory. *Phys. Rev. Lett.*, 89:011301, Jun 2002.

[12] Joachim Kopp. Phenomenology of Three-Flavour Neutrino Oscillations. `http://www.mpi-hd.mpg.de/phenocond/pdf/diploma-thesis.pdf`.

[13] Maki Ziro, Nakagawa Masami, and Sakata Shoichi. Remarks on the unified model of elementary particles. *Prog.Theor.Phys.*, 28:870–880, 1962.

[14] J.K. Ahn et al. Observation of Reactor Electron Antineutrino Disappearance in the RENO Experiment. *Phys.Rev.Lett.*, 108:191802, 2012.

[15] Y. Abe et al. Direct measurement of backgrounds using reactor-off data in double chooz. *Phys. Rev.*, D87:011102, 2013.

[16] A. Hummada, S. Lazrak Mikou, G. Bagieu, J.F. Cavaignac, and Dy. Holm Koang. Neutrino oscillations i.l.l. experiment reanalysis. *Applied Radiation and Isotopes*, 46:449–450, 1995.

[17] F. H. Boehm et al. Experimental study of neutrino oscillations at a fission reactor. *Phys. Lett.*, B97:310–314, 1980.

[18] B. Achkar et al. Search for neutrino oscillations at 15-meters, 40-meters, and 95-meters from a nuclear power reactor at bugey. *Nucl. Phys.*, B434:503–534, 1995.

[19] J. F. Cavaignac et al. Indication for neutrino oscillation from a high statistics experiment at the bugey reactor. *Phys. Lett.*, B148:387–394, 1984.

[20] C. Bemporad. A long-base search for neutrino oscillations at a reactor: The chooz experiment. 1997. Given at International Europhysics Conference on High-Energy Physics (HEP 97), Jerusalem, Israel, 19-26 Aug 1997.

[21] M. Apollonio et al. Initial results from the chooz long baseline reactor neutrino oscillation experiment. *Phys. Lett.*, B420:397–404, 1998.

[22] F. Boehm et al. Search for neutrino oscillations at the palo verde nuclear reactors. *Phys. Rev. Lett.*, 84:3764–3767, 2000.

[23] K. Eguchi et al. First results from kamland: Evidence for reactor anti-neutrino disappearance. *Phys. Rev. Lett.*, 90:021802, 2003.

[24] S. Abe et al. Precision measurement of neutrino oscillation parameters with kamland. *Phys. Rev. Lett.*, 100:221803, 2008.

[25] F. Boehm et al. Results from the palo verde neutrino oscillation experiment. *Phys. Rev.*, D62:072002, 2000.

[26] K. Heeger, P. Huber, C. Lewis, M. McFarlane, and W. Wang. Study of the Sensitivity of the Daya Bay Reactor Neutrino Experiment to $sin^2 2\theta_{13}$ Using GLoBES. In *APS Meeting Abstracts*, October 2009.

[27] The Daya Bay collaboration. A side-by-side comparison of Daya Bay antineutrino detectors. *Nucl.Instrum.Meth.*, A685:78–97, 2012.

[28] The Daya Bay Collaboration. A Precision Measurement of the Neutrino Mixing Angle $\theta_{13}$ using Reactor Antineutrinos at Daya Bay.

[29] M. Yeh, A. Garnov, and Richard L. Hahn. Gadolinium-loaded liquid scintillator for high-precision measurements of antineutrino oscillations and the mixing angle, Theta(13). *Nucl.Instrum.Meth.*, A578:329–339, 2007.

[30] J. A. Formaggio and G. P. Zeller. From ev to eev: Neutrino cross sections across energy scales. *Rev. Mod. Phys.*, 84:1307–1341, Sep 2012.

[31] Dupont. Technical information of Tyvek. `http://www2.dupont.com/Tyvek/en_US/tech_info/test_results.html`.

[32] G. Giacomelli and A. Margiotta. The MACRO Experiment at Gran Sasso. `http://arxiv.org/abs/0707.1691`.

[33] F.P. An et al. The muon system of the daya bay reactor antineutrino experiment. 2014.

[34] Qingmin Zhang, Yifang Wang, Jiawen Zhang, Jun Cao, Talent Kwok, et al. An underground cosmic-ray detector made of RPC. *Nucl.Instrum.Meth.*, A583:278–284, 2007.

[35] Ji-Lei Xu, Meng-Yun Guan, Chang-Gen Yang, Yi-Fang Wang, Jia-Wen Zhang, et al. Design and preliminary test results of Daya Bay RPC modules. *Chin.Phys.*, C35:844–850, 2011.

[36] Hanxiong Huang et al. Manual calibration system for daya bay reactor neutrino experiment. *JINST*, 8:P09013, 2013.

[37] DYB collaboration. Automated Calibration System for Daya Bay Experiment. `http://dayabay.ihep.ac.cn/cgi-bin/DocDB/ShowDocument?docid=8957`.

[38] J. Ling, X. Qian, W. Wang, and Z. Chao. BCW Rate+Shape Analysis Technote. `http://dayabay.ihep.ac.cn/cgi-bin/DocDB/ShowDocument?docid=8768`.

[39] X. Qian and F. Wu. ACU source spectrum and rate. `http://dayabay.ihep.ac.cn/DocDB/0072/007264/001/source_spectrum.pdf`.

[40] Jianglai Liu. Automated Calibration System for Daya Bay Experiment. `http://dayabay.ihep.ac.cn/cgi-bin/DocDB/ShowDocument?docid=8326`.

[41] S. Jetter. Technote: Review of the IHEP non-linearity model. `http://dayabay.ihep.ac.cn/cgi-bin/DocDB/ShowDocument?docid=8995`.

[42] Dan Dwyer. Spectral Measurement of Oscillation at Daya Bay. `http://dayabay.ihep.ac.cn/cgi-bin/DocDB/ShowDocument?docid=9216`.

[43] Yue Meng. Pool PMT timing calibration. `http://dayabay.ihep.ac.cn/cgi-bin/DocDB/ShowDocument?docid=7696`.

[44] DuPont Inc. General properties of Teflon FEP. www.rjchase.com/fep_handbook.pdf.

[45] Daya Bay Collaboration. Muon Dry Run results. http://dayabay.ihep.ac.cn/cgi-bin/DocDB/ShowDocument?docid=5946.

[46] Daya bay Collaboration. Commissioning of RPC detector systems at Daya Bay Reactor Neutrino Experiment. http://dayabay.ihep.ac.cn/cgi-bin/DocDB/ShowDocument?docid=8505.

[47] Q. He and Z. Wang. Rolling gain note. http://dayabay.ihep.ac.cn/cgi-bin/DocDB/ShowDocument?docid=7198.

[48] H. Lu. Water attneuation length study. http://dayabay.ihep.ac.cn/cgi-bin/DocDB/ShowDocument?docid=7948.

[49] V. Kopeikin, L. Mikaelyan, and V. Sinev. Antineutrino background from spent fuel storage in sensitive searches for theta(13) at reactors. *Phys.Atom.Nucl.*, 69:185–188, 2006.

[50] P. Huber. Spent fuel neutrinos. http://dayabay.ihep.ac.cn/cgi-bin/DocDB/ShowDocument?docid=8666.

[51] Bin Zhou, Xi-Chao Ruan, Yang-Bo Nie, Zu-Ying Zhou, Feng-Peng An, et al. A study of antineutrino spectra from spent nuclear fuel at Daya Bay. *Chin.Phys.*, C36:1–5, 2012.

[52] Cao Jun. Study of PMT flasher. http://dayabay.ihep.ac.cn/cgi-bin/DocDB/ShowDocument?docid=6956.

[53] F. P. An et al. Observation of electron-antineutrino disappearance at daya bay. *Phys. Rev. Lett.*, 108:171803, 2012.

[54] Zhang Chao. Accidentals distribution in IBD candiates. http://dayabay.ihep.ac.cn/cgi-bin/DocDB/ShowDocument?docid=7309.

[55] KV. Tsang. P14A fast neutron background. http://dayabay.ihep.ac.cn/cgi-bin/DocDB/ShowDocument?docid=9819.

[56] Ochoa Pedro. Accidentals distribution in IBD candidates. http://dayabay.ihep.ac.cn/cgi-bin/DocDB/ShowDocument?docid=8860.

[57] Yu Zeyuan. Alpha-n background in P14A analysis. http://dayabay.ihep.ac.cn/cgi-bin/DocDB/ShowDocument?docid=9667.

[58] C. Lewis. P12E reactor data/prediction comparison. http://dayabay.ihep.ac.cn/cgi-bin/DocDB/ShowDocument?docid=9507.

[59] Patrick Huber. On the determination of anti-neutrino spectra from nuclear reactors. *Phys.Rev.*, C84:024617, 2011.

[60] Y. Nakajima and D. Dwyer. A note on L/E figure. http://dayabay.ihep.ac.cn/cgi-bin/DocDB/ShowDocument?docid=9220.

[61] Q. Zhao. Spectrum unfolding summary. http://dayabay.ihep.ac.cn/cgi-bin/DocDB/ShowDocument?docid=9678.

[62] Q. Zhao W. Zhong and F. An. Daya Bay Generic Anti-neutrino Spectrum Measurement TechNote. http://dayabay.ihep.ac.cn/cgi-bin/DocDB/ShowDocument?docid=9345.

[63] F.P. An et al. Spectral measurement of electron antineutrino oscillation amplitude and frequency at Daya Bay. *Phys.Rev.Lett.*, 112:061801, 2014.

[64] C. Lewis. Comparison of spectrum to prediction. http://dayabay.ihep.ac.cn/cgi-bin/DocDB/ShowDocument?docid=9613.

[65] Michel Cribier. Reactor monitoring with neutrinos. *Nucl.Phys.Proc.Suppl.*, 221:57–61, 2011.

[66] J. Ling and Y. Nakajima. Daya Bay Sterile Neutrino Workshop. `http://dayabay.ihep.ac.cn/cgi-bin/DocDB/ShowDocument?docid=9705`.

[67] nH analysis group. nGd+nH combination. `http://dayabay.ihep.ac.cn/cgi-bin/DocDB/ShowDocument?docid=9543`.

[68] DYB collaboration. Supernova early warning in DYB experiment. `http://dayabay.ihep.ac.cn/cgi-bin/DocDB/ShowDocument?docid=9301`.

[69] K. Abe et al. Precise measurement of the neutrino mixing parameter $\theta_{23}$ from muon neutrino disappearance in an off-axis beam. *Phys.Rev.Lett.*, 112:181801, 2014.

[70] R.B. Patterson. The NOvA Experiment: Status and Outlook. *Nucl.Phys.Proc.Suppl.*, 235-236:151–157, 2013.

[71] LBNE collaboration. The Long-Baseline Neutrino Experiment: Exploring Fundamental Symmetries of the Universe. `http://arxiv.org/abs/1307.7335`.

[72] LENA collaboration. The Physics Potential of the LENA Detector. `http://arxiv.org/abs/1004.3474`.

[73] HyperK collaboration. Letter of Intent: The Hyper-Kamiokande Experiment — Detector Design and Physics Potential. `http://arxiv.org/abs/1109.3262`.

[74] Carl H. Albright. Overview of Neutrino Mixing Models and Ways to Differentiate among Them. pages 91–109, 2009.

[75] Pouya Bakhti and Yasaman Farzan. Constraining Super-light Sterile Neutrino Scenario by JUNO and RENO-50. *JHEP*, 1310:200, 2013.

[76] J. Park. Study of Neutrino Mass Hierarchy with RENO-50. *PoS*, Neutel2013:076, 2013.